IMAGES. III. The evolution of the near-infrared Tully-Fisher relation over the last 6 Gyr

M. Puech, H. Flores, F. Hammer, Y. Yang, B. Neichel, M. Lehnert, L. Chemin, N. Nesvadba, B. Epinat, P. Amram, et al.

A&A 484, 173–187 (2008)
DOI: 10.1051/0004-6361:20079313

Astronomy & Astrophysics

IMAGES

III. The evolution of the near-infrared Tully-Fisher relation over the last 6 Gyr⋆

M. Puech[1,2], H. Flores[2], F. Hammer[2], Y. Yang[2], B. Neichel[2], M. Lehnert[2], L. Chemin[2], N. Nesvadba[2], B. Epinat[5], P. Amram[5], C. Balkowski[2], C. Cesarsky[1], H. Dannerbauer[6], S. di Serego Alighieri[7], I. Fuentes-Carrera[2], B. Guiderdoni[8], A. Kembhavi[3], Y. C. Liang[9], G. Östlin[10], L. Pozzetti[4], C. D. Ravikumar[11], A. Rawat[2,3], D. Vergani[12], J. Vernet[1], and H. Wozniak[8]

[1] ESO, Karl-Schwarzschild-Strasse 2, 85748 Garching bei München, Germany
e-mail: mpuech@eso.org
[2] GEPI, Observatoire de Paris, CNRS, University Paris Diderot, 5 Place Jules Janssen, 92190 Meudon, France
[3] Inter-University Centre for Astronomy and Astrophysics, Post Bag 4, Ganeshkhind, Pune 411007, India
[4] INAF – Osservatorio Astronomico di Bologna, via Ranzani 1, 40127 Bologna, Italy
[5] Laboratoire d'Astrophysique de Marseille, Observatoire Astronomique de Marseille-Provence, 2 Place Le Verrier, 13248 Marseille, France
[6] MPIA, Königstuhl 17, 69117 Heidelberg, Germany
[7] INAF – Osservatorio Astrofisico di Arcetri, Largo Enrico Fermi 5, 50125 Florence, Italy
[8] Centre de Recherche Astronomique de Lyon, 9 Avenue Charles André, 69561 Saint-Genis-Laval Cedex, France
[9] National Astronomical Observatories, Chinese Academy of Sciences, 20A Datun Road, Chaoyang District, Beijing 100012, PR China
[10] Stockholm Observatory, AlbaNova University Center, Stockholms Center for Physics, Astronomy and Biotechnology, Roslagstullsbacken 21, 10691 Stockholm, Sweden
[11] Department of Physics, University of Calicut, Kerala 673635, India
[12] IASF – INAF, via Bassini 15, 20133 Milano, Italy

Received 21 December 2007 / Accepted 17 March 2008

ABSTRACT

Using the multi-integral field spectrograph GIRAFFE at VLT, we have derived the K-band Tully-Fisher relation (TFR) at $z \sim 0.6$ for a representative sample of 65 galaxies with emission lines (W_0(OII) $\geq$ 15 Å). We confirm that the scatter in the $z \sim 0.6$ TFR is caused by galaxies with anomalous kinematics, and find a positive and strong correlation between the complexity of the kinematics and the scatter that they contribute to the TFR. Considering only relaxed-rotating disks, the scatter, and possibly also the slope, of the TFR, do not appear to evolve with redshift. We detect an evolution of the K-band TFR zero point between $z \sim 0.6$ and $z = 0$, which, if interpreted as an evolution of the K-band luminosity of rotating disks, would imply that a brightening of 0.66 ± 0.14 mag occurs between $z \sim 0.6$ and $z = 0$. Any disagreement with the results of Flores et al. (2006, A&A, 455, 107) are attributed to both an improvement of the local TFR and the more detailed accurate measurement of the rotation velocities in the distant sample. Most of the uncertainty can be explained by the relatively coarse spatial-resolution of the kinematical data. Because most rotating disks at $z \sim 0.6$ are unlikely to experience further merging events, one may assume that their rotational velocity, which is taken as a proxy of the total mass, does not evolve dramatically. If true, our result implies that rotating disks observed at $z \sim 0.6$ are rapidly transforming their gas into stars, to be able to double their stellar masses and be observed on the TFR at $z = 0$. The rotating disks observed are indeed emission-line galaxies that are either starbursts or LIRGs, which implies that they are forming stars at a high rate. Thus, a significant fraction of the rotating disks are forming the bulk of their stars within 6 to 8 Gyr, in good agreement with former studies of the evolution of the mass-metallicity relationship.

Key words. galaxies: evolution – galaxies: kinematics and dynamics – galaxies: high-redshift – galaxies: general – galaxies: interactions – galaxies: spiral

1. Introduction

Since the first rotation curves were measured at intermediate redshifts (Vogt et al. 1993), many studies have been devoted to the evolution of the Tully-Fisher Relation (TFR, Tully & Fisher 1977), given its prominent role in constraining galaxy-formation models (e.g., Dutton et al. 2007). Early work using B-band imaging found only modest luminosity evolution (Vogt et al. 1996, 1997), but subsequent studies using data of the same band have suggested a more significant evolution (Simard & Pritchet 1998; Bamford et al. 2006; Weiner et al. 2006; Chiu et al. 2007). In almost all of these studies, the B-band TFR shows a large dispersion in comparison with the local relation, especially at the low-luminosity (or velocity) end (e.g., Böhm et al. 2004). Böhm & Ziegler (2007) showed that this effect could be attributed to an incompleteness in magnitude provided that the scatter decreased by a factor of at least three between $z \sim 0.5$ and $z = 0$, with no evolution of slope or zero point. Alternatively, they proposed a possible luminosity-dependent evolution, in which distant low-luminosity galaxies would have lower mass-to-light ratios $[M/L]$

⋆ Intermediate MAss Galaxy Evolution Sequence, ESO programs 174.B-0328(A), 174.B-0328(E).

than their local counterparts, while higher-luminosity galaxies would not undergo strong M/L evolution. Therefore, the situation for B-band data remains unclear, particularly concerning the large scatter in measurements found at high redshift.

To minimize observational biases and enable easier comparisons with models, a progressive interest has been devoted to the K-band and stellar-mass TFRs (hereafter, smTFR). Long-slit spectroscopy of distant galaxies revealed an smTFR of significant scatter, with detectable evolution of neither zero point nor slope, up to $z \sim 1$ (Conselice et al. 2005). This much larger dispersion appears to be linked to "kinematically anomalous galaxies", as inferred from local studies (Kannappan & Barton 2004), or, from a morphological point of view, with disturbed, compact, or merging galaxies (Kassin et al. 2007; Atkinson et al. 2007). Weiner et al. (2006) and Kassin et al. (2007) defined a new tracer of the galaxy dark-halo potential called S, which corrects the rotation velocity for disordered, non-circular motions. Once expressed using this new kinematical estimator, the distant smTFR shows significantly-reduced scatter, with no detectable evolution in either zero point or slope. This suggests an important role of non-ordered motions in increasing the scatter of the distant TFR.

In this respect, 3D spectroscopy provides a unique way to distinguish relaxed rotating disks from other kinematically-disturbed galaxies. Kinematically-selected relaxed (or pure) rotating disks at $z \sim 0.6$ present a TFR that appears to evolve neither in slope, zero point, nor *dispersion* (Flores et al. 2006): kinematically-anomalous galaxies, which range from perturbed rotators where a rotation can be detected to galaxies with complex kinematics but no noticeable rotation, appear to be responsible for the increased scatter of the distant TFR. Therefore, 3D spectroscopy allows us to establish a direct connection between non-ordered motions and kinematical and morphological anomalies. In this paper, we double the sample previously available (see Yang et al. 2007, hereafter Paper I) to test robustly the results obtained in Flores et al. (2006).

This paper is organized as follows: Sect. 2 introduces the data used in this study; Sect. 3 details the methodology used for the analysis; Sect. 4 presents the K-band TFR obtained from GIRAFFE data, and Sect. 5 draws the conclusions from this work. In the Appendix, we derive the stellar-mass TFR in the GIRAFFE sample. Throughout, we adopt $H_0 = 70\ \mathrm{km\,s^{-1}\,Mpc^{-1}}$, $\Omega_\mathrm{M} = 0.3$, and $\Omega_\Lambda = 0.7$, and the AB magnitude system.

2. Data

2.1. Distant sample

2.1.1. Kinematics

We used the multi-object integral field spectrograph FLAMES-GIRAFFE at VLT, to obtain the [OII] spatially-resolved kinematics of a sample of 68 galaxies at $0.4 \leq z \leq 0.75$. The median redshift of the sample was $z_\mathrm{med} \sim 0.61$, which corresponds to a look-back time ~5.8 Gyr, while the 25 and 75 percentiles of the redshift distribution are $z_{25} \sim 0.49$ and $z_{75} \sim 0.67$. This sample represents well the luminosity function of $z \sim 0.6$ galaxies with stellar masses [M_stellar] in the $1.5{-}15\times10^{10}\ M_\odot$ range, and is unaffected by field-to-field variations within Poisson statistics, as targets were observed in four different fields (see Paper I).

Flores et al. (2006) and Paper I used GIRAFFE velocity fields [VF] and velocity dispersion maps [σ-maps], to define three kinematical classes, namely the *rotating disks* [RD], which correspond to relaxed rotators, the *perturbed rotators* [PR], corresponding to rotating disks showing some weak disturbances, and *kinematically-complex* [CK] galaxies, corresponding to dynamically non-relaxed galaxies, probably associated with major mergers (see also Puech et al. 2006a, 2007a). This classification takes into account the residuals between the observed VF and σ-map and those predicted by a rotating-disk model (see Paper I), which mitigates the subjectivity of a fully visual classification.

2.1.2. Morphology

A detailed morphological analysis of a subsample of 52 galaxies, which had multi-band HST/ACS imaging data, was completed by Neichel et al. (2008, hereafter, Paper II). They found a good agreement between both kinematical and morphological classifications. Only 16% of galaxies in this subsample are both kinematically-classified as RDs and morphologically-classified as spirals. These "rotating spiral disks" were selected to have a redder bulge than the disk and to be therefore quite similar to local spirals, apart their much bluer integrated colors and [OII] equivalent widths (see Paper II, for a detailed discussion). Furthermore, they showed no special trend in size nor in Bulge-to-Total luminosity ratio [B/T] compared to local galaxies, and we do not expect any bias in the distant TFR that could be due to morphological variation of the TFR along the Hubble Sequence (see, e.g., Russell 2004). In the following, we use the inclinations [i] and half light radii [R_half] derived in Paper II.

The comparison between kinematics and morphology revealed two special cases of RDs. First, J033230.78-275455.0 was detected in emission only on one half of the galaxy, which was caused by the superposition of a skyline on an [OII] emission line. This galaxy was classified as a RD, but the amplitude of its VF is affected by large uncertainty. Second, J033241.88-274853.9 was classified as a Tadpole galaxy in Paper II because of its highly-asymmetric shape. In the following (see Sect. 3.2), we assume that all RD flux distributions can be approximated by an exponential disk, which, obviously, does not apply to this galaxy. Therefore, in this paper, "RDs" refers to galaxies classified as rotating disks in Paper I *excluding* J033230.78-275455.0 and J033241.88-274853.9, while "RD+" refers to all RDs *including* J033230.78-275455.0 and J033241.88-274853.9.

2.1.3. Absolute K-band magnitudes

Absolute K-band magnitudes M_K were taken from Flores et al. (2006) and Ravikumar et al. (2007). They were derived using Bruzual & Charlot 2001 stellar-population models, assuming a CSP template with solar metallicity and an exponential star-formation history with $\tau = 0.5$ Gyr, which describes the properties of most galaxies between $z = 0.4$ and 1 (Hammer et al. 2001). For each galaxy, an optimal SED was found by matching the observed $J - K$ color. This method was preferred to complete SED fitting because 50% of the selected galaxies, from the CFRS and the HDFS, did not have similar multiwavelength photometric data to galaxies in the remaining 50%, which were selected from the CDFS; SED fitting would, therefore, not have been able to measure an M_K of similar quality for all galaxies studied. We compared, for galaxies from the CDFS, the impact of this simple "color-matching" method relatively to a full SED fitting (using optical photometry only): we found an excellent agreement between J-band absolute magnitudes with a $1{-}\sigma$ dispersion ~0.01 mag, and no systematic effect (Hammer & Pozzetti, private communication). We compared absolute J-band and not K-band magnitudes because whatever the method used,

these are not extrapolations. A potential drawback of the "color-matching" method is that M_K is extrapolated, since the reddest photometric point used is the observed K-band, which falls roughly in the middle of the rest-frame J and H band at $z \sim 0.6$. For galaxies in the CDFS, IRAC 3.6 μm fluxes were publicly available, which allowed us to compare the M_K obtained using this method with those obtained taking into account the IR 3.6 μm flux: we found a residual $1-\sigma$ dispersion of 0.12 mag between both estimates, with no systematic effect. Using two independent photometric datasets for galaxies in the CDFS (i.e., EIS and ACS), we derived a random uncertainty of $\lesssim$0.2 mag on M_K, with no noticeable systematic uncertainties. Therefore, we adopted a random uncertainty of 0.2 mag and neglected systematic uncertainties.

Absolute magnitudes were corrected for internal extinction, using the mass-dependent method of Tully et al. (1998). We applied an additional correction of 0.04 mag that accounted for extinction in face-on galaxies (Tully et al. 1998, 1985). We note that within the sample of 68 objects, three do not have NIR photometry (see Table 1).

2.1.4. Summary

For the distant sample, all measurements used are listed in Table 1. The columns of the table are as follows: (1) IAU ID, (2) Internal ID, (3) Redshift z, (4) Inclination i (in deg, ±5 deg, see Sect. 2.1.2), (5) Dynamical Class D.C., (6) Projected radial velocity $\Delta V_{\rm obs} \sin(i)$ (in km s^{-1}, see Sect. 3.1), (7) Rotation velocity corrected for inclination and spatial-resolution effects $V_{\rm flat}$ (in km s^{-1}, see Sect. 3.1), (8) Total uncertainty in $V_{\rm flat}$ (in km s^{-1}, see Sect. 3.4), (9) Absolute K-band magnitude M_K (uncorrected for extinction), (10) Absolute K-band magnitude M_K^c corrected for extinction (±0.2 mag, see Sect. 2.1.3), and (11) Stellar mass in $\log(M_{\rm stellar}/M_\odot)$ (±0.3 dex, see Appendix A).

2.2. Local sample

As a local reference, we adopt the K-band TFR derived by Hammer et al. (2007) for a complete subsample of the SDSS (Pizagno et al. 2007), which allows us to control systematic effects that can occur when comparing local and distant samples.

One important choice for studying the TFR is the kinematical estimator used for the rotation velocity $V_{\rm rot}$. Studies of the local TFR have shown that using different estimators (e.g., the maximal rotation velocity $V_{\rm max}$, the plateau rotation curve velocity $V_{\rm flat}$, the velocity measured at the radius containing 80% of the light V_{80}, and the velocity $V_{2.2}$ measured at 2.2 disk scale length) can lead to different results (see, e.g., Verheijen 2001; Pizagno et al. 2007). $V_{\rm flat}$ has been shown to be correlated with $V_{\rm rot}$, since it is less influenced by the bulge dynamics, which can produce a central "bump" with $V_{\rm max} > V_{\rm flat}$. This can then lead to a tighter TF relation (e.g., Verheijen 2001), and a significant improvement in the linearity of the K-band relation at the high-mass end (Noordermeer & Verheijen 2007). For the local sample, we adopted the V_{80} measurements of Pizagno et al. (2007) using arctan fits to the RCs. To limit uncertainties, we restricted the local sample to galaxies for which V_{80} is a good proxy for $V_{\rm flat}$ (i.e., Pizagno et al. 2007, flags 1 and 2), as shown by Hammer et al. (2007).

Rotation velocities were corrected for inclination using estimates derived from their morphological axis ratio. When well-resolved 2D kinematics is available, it is possible to derive the inclination directly from the fit of the VF. However, large differences (up to ∼10 deg) can be found between such kinematically-derived inclinations and the ones inferred from the morphological axis ratio (e.g., Chemin et al. 2006). Since we do not have 2D kinematics for galaxies in the local sample, we use morphologically-derived inclinations exclusively. This provides us with homogeneous estimates for the local and distant samples, since in the latter we also use such inclinations.

Hammer et al. (2007) combined the Pizagno et al. (2007) kinematic measurements with 2MASS $K_{\rm s}$-photometry. We estimated absolute magnitudes in the local sample following a similar method to that used for the distant sample, including corrections for extinctions (see Sect. 2.1.3). The 2MASS $K_{\rm s}$ filter has the advantage of being close to the ISAAC $K_{\rm s}$ filter used in the distant sample. Both filters match well the K-band LCO filter designed to establish the faint IR standard-star system of Persson et al. (1998) (Mason et al. 2007; Carpenter 2001). We assumed that both filters are identical during the SED-fitting procedure, which did not introduce any systematic effect. We note than 2MASS K-band magnitudes were converted into AB magnitudes using $K_{\rm s}({\rm AB}) = K_{\rm s}({\rm Vega}) + 1.85$, following Blanton et al. (2005).

Since we are exploring the higher tail of the stellar-mass distribution and the TFR is highly sensitive to stellar mass (see, e.g., McGaugh 2005), we restrict the K-band TFR to $\log(V_{\rm flat}) \geq 2.2$ and find from Hammer et al. (2007):

$$M_K({\rm AB}) = -6.54 \pm 1.33 - (6.88 \pm 0.57) \times \log(V_{\rm flat}), \quad (1)$$

with a residual dispersion $\sigma_{\rm res} = 0.38$ mag. Since we used uniform M_K error bars, we used direct fits to the TFR, i.e., with M_K as a $V_{\rm flat}$-dependent variable (using the IDL MPFITFUN procedure of Markwardt, translated from the MINPACK-1 package[1]).

3. Methodology

3.1. Derivation of the rotation velocity

For each galaxy, we estimated the deprojected VF half-amplitude using $\Delta V_{\rm obs} = (V_{\rm max}^{\rm IFU} - V_{\rm min}^{\rm IFU})/(2\sin(i))$, where $V_{\rm max}^{\rm IFU}$ and $V_{\rm min}^{\rm IFU}$ are respectively the maximal and minimal values of the VF sampled by the IFU (see Table 1).

Because of the influence of the relatively coarse spatial-resolution of the kinematic data, $\Delta V_{\rm obs}$ underestimates the true rotation velocity $V_{\rm rot}$ (see Flores et al. 2006; Puech et al. 2006a). Rather than applying a mean correction factor to the entire sample as in Flores et al. (2006), we corrected each galaxy *individually* by modeling its data-cube. We used a method developed from that used by Flores et al. (2006) and in Paper I, to model the σ-map. Assuming that all galaxies are thin-rotating disks, we modeled their data-cube, from their observed VF and σ-map, in the following way.

First, for each galaxy, we constructed a grid of rotation curves (RC) with $V_{\rm rot}$ spaced at 10 km s^{-1} intervals, which roughly corresponded to the typical uncertainty in $\Delta V_{\rm obs}$ (see Sect. 3.4). Because of a lack of spatial resolution, the precise shape of distant RCs remains largely unknown. Therefore, we chose a simple arctan defined as $V_0 \times (2/\pi) \times \arctan(r/r_{\rm t})$, which depends only on two parameters, i.e., the asymptotic velocity V_0, and the "turnover" radius $r_{\rm t}$ (see, e.g., Courteau 1997). This RC shape was used in Paper I to model the VF of each distant galaxy. In the RD+ subsample, such models provided good matches to the observed VFs, which demonstrated that such a

[1] http://cow.physics.wisc.edu/~craigm/idl/mpfittut.html

Table 1. Principle properties of the sample of 68 galaxies used in this study, ordered by increasing RA (see text).

IAU ID	Internal ID	z	i	DC	$\Delta V_{\rm obs} \sin(i)$	$V_{\rm flat}$	$\Delta V_{\rm flat}$	M_K	M_K^c	$\log(M_{\rm stellar}/M_\odot)$
J030225.28+001325.1	CFRS030085	0.6100	71	RD	127	170	23	–20.83	–20.98	10.21
J030228.72+001333.9	CFRS030046	0.5120	66	RD	148	200	29	–21.68	–21.82	10.64
J030232.16+000639.1	CFRS039003	0.6189	29	RD	110	290	79	99.99	99.99	99.99
J030238.74+000611.5	CFRS031032	0.6180	37	PR	83	200	36	–22.64	–22.70	11.00
J030239.38+001327.1	CFRS030523	0.6508	41	CK	63	130	38	–21.55	–21.61	10.48
J030240.45+001359.4	CFRS030508	0.4642	38	CK	47	100	40	–20.34	–20.40	10.00
J030240.99+000655.4	CFRS031016	0.7054	67	CK	15	30	25	–21.24	–21.25	10.37
J030242.19+001324.3	CFRS030488	0.6069	41	CK	36	70	36	–20.84	–20.89	10.20
J030245.67+001027.9	CFRS030645	0.5275	45	CK	89	150	38	–21.34	–21.42	10.40
J030246.94+001032.6	CFRS030619	0.4854	27	RD	70	210	76	–21.93	–21.99	10.63
J030248.41+000916.5	CFRS031353	0.6340	57	RD	174	260	41	–22.42	–22.54	10.85
J030249.10+001002.1	CFRS031349	0.6155	48	PR	175	290	46	–22.92	–23.01	11.04
J030252.03+001033.4	CFRS031309	0.6170	71	CK	84	150	22	–22.91	–23.05	11.03
J033210.25-274819.5	CDFS4301297	0.6100	69	PR	110	150	26	–20.83	–20.96	10.29
J033210.76-274234.6	CDFS4402679	0.4180	26	CK	186	550	123	–23.62	–23.68	11.44
J033212.39-274353.6	CDFS3400803	0.4230	90	RD	105	180	22	–21.55	–21.85	10.61
J033213.06-274204.8	CDFS3500001	0.4220	79	CK	90	130	22	–20.56	–20.73	10.19
J033214.97-275005.5	CDFS3300063	0.6680	22	PR	62	190	90	–22.45	–22.50	10.92
J033217.62-274257.4	CDFS3401109	0.6470	46	CK	131	250	43	–21.15	–21.24	10.38
J033219.32-274514.0	CDFS3400329	0.7250	72	CK	116	270	29	–21.16	–21.36	10.39
J033219.61-274831.0	CDFS3300651	0.6710	49	PR	82	190	33	–20.90	–20.98	10.27
J033219.68-275023.6	CDFS3202670	0.5610	58	RD	161	230	33	–22.30	–21.42	10.88
J033220.48-275143.9	CDFS3202141	0.6790	63	CK	39	70	24	–20.63	–20.70	10.18
J033224.60-274428.1	CDFS3400618	0.5380	65	CK	63	90	27	–20.35	–20.44	10.08
J033225.26-274524.0	CDFS3400279	0.6660	60	CK	47	80	26	–21.54	–21.61	10.56
J033226.23-274222.8	CDFS3401338	0.6679	76	PR	150	200	24	–21.93	–22.13	10.72
J033227.07-274404.7	CDFS3400743	0.7390	84	CK	71	110	21	–20.95	–21.15	10.26
J033228.48-274826.6	CDFS3300684	0.6697	22	CK	23	130	66	–21.68	–21.73	10.63
J033230.43-275304.0	CDFS2200433	0.6460	70	CK	219	380	29	–21.68	–21.90	10.64
J033230.57-274518.2	CDFS2400243	0.6810	34	CK	41	80	46	–22.86	–22.91	11.08
J033230.78-275455.0	CDFS2102060	0.6870	66	RD+	90	200	43	–21.82	–21.96	10.66
J033231.58-274121.6	CDFS2500322	0.7047	42	RD	81	140	41	–20.51	–20.57	10.10
J033232.96-274106.8	CDFS2500425	0.4690	16	PR	31	210	117	–20.13	–20.17	10.01
J033233.90-274237.9	CDFS2401349	0.6190	17	PR	46	200	107	–21.82	–21.96	10.66
J033234.04-275009.7	CDFS2300055	0.7030	59	RD	104	160	29	–20.50	–20.60	10.09
J033234.12-273953.5	CDFS2500971	0.6280	32	CK	25	110	44	99.99	99.99	99.99
J033237.54-274838.9	CDFS2300477	0.6650	31	RD	106	230	71	–21.98	–22.03	10.70
J033238.60-274631.4	CDFS2301047	0.6220	60	RD	118	210	33	–21.45	–21.57	10.53
J033239.04-274132.4	CDFS2500233	0.7330	43	PR	58	130	39	–20.62	–20.68	10.14
J033239.72-275154.7	CDFS2200829	0.4160	35	CK	16	30	36	–20.94	–20.98	10.31
J033240.04-274418.6	CDFS2400536	0.5223	16	CK	108	470	214	–21.95	–22.00	10.77
J033241.88-274853.9	CDFS2300404	0.6680	67	RD+	80	120	27	–20.90	–21.01	10.27
J033243.62-275232.6	CDFS2200611	0.6800	71	PR	38	60	23	–19.94	–20.01	9.86
J033244.20-274733.5	CDFS2300750	0.7365	39	CK	46	170	40	–21.76	–21.83	10.62
J033245.11-274724.0	CDFS2300800	0.4360	43	RD	95	270	44	–22.03	–22.11	10.80
J033248.28-275028.9	CDFS1202537	0.4462	81	PR	76	110	22	–20.38	–20.54	10.09
J033249.53-274630.0	CDFS1302369	0.5230	46	PR	74	150	39	–21.00	–21.07	10.34
J033250.24-274538.9	CDFS1400714	0.7318	31	CK	82	240	67	–20.59	–20.65	10.12
J033250.53-274800.7	CDFS1301018	0.7370	62	PR	71	110	26	–20.34	–20.43	10.01
J221741.46+001854.8	CFRS221119	0.5138	41	RD	135	250	47	99.99	99.99	99.99
J221743.08+001508.3	CFRS221064	0.5383	48	PR	93	250	29	–21.64	–22.74	10.53
J221745.12+001447.4	CFRS220975	0.4211	50	CK	313	410	44	–22.53	–22.64	10.95
J221746.48+001653.5	CFRS220919	0.4738	60	CK	39	30	23	–19.53	–19.55	9.67
J221754.56+001900.3	CFRS220619	0.4676	68	PR	62	90	24	–19.33	–19.42	9.63
J221758.07+002137.5	CFRS220504	0.5379	42	RD	93	170	42	–21.36	–21.43	10.43
J221802.92+001428.0	CFRS220321	0.4230	42	PR	104	220	46	–20.79	–20.87	10.21
J221803.55+002131.9	CFRS220293	0.5420	45	CK	89	160	40	–20.89	–20.97	10.24

Table 1. continued.

IAU ID	Internal ID	z	i	DC	$\Delta V_{\rm obs} \sin(i)$	$V_{\rm flat}$	$\Delta V_{\rm flat}$	M_K	M_K^c	$\log(M_{\rm stellar}/M_\odot)$
J223241.45-603516.1	HDFS4130	0.4054	36	CK	90	220	53	–22.13	–22.20	10.76
J223245.56-603418.8	HDFS4170	0.4602	51	RD	134	230	37	–22.60	–22.70	10.96
J223252.74-603207.3	HDFS4040	0.4650	51	PR	75	120	32	–20.04	–20.11	9.88
J223254.05-603251.6	HDFS4090	0.5162	45	CK	14	20	30	–19.83	–19.85	9.80
J223256.07-603148.8	HDFS4020	0.5138	50	RD	88	140	36	–20.12	–20.20	9.96
J223256.08-603414.1	HDFS5140	0.5649	50	CK	171	220	42	–20.46	–20.56	10.04
J223257.52-603305.9	HDFS5030	0.5821	25	CK	31	130	69	–22.68	–22.73	10.94
J223258.01-603525.9	HDFS4180	0.4647	64	RD	104	140	26	–20.38	–20.49	10.04
J223258.23-603331.4	HDFS4070	0.4230	40	CK	36	70	43	–19.67	–19.72	9.75
J223300.09-603529.9	HDFS5190	0.6952	59	RD	144	230	23	–21.92	–22.04	10.64
J223302.45-603346.5	HDFS5150	0.6956	42	PR	51	120	39	–21.02	–21.09	10.27

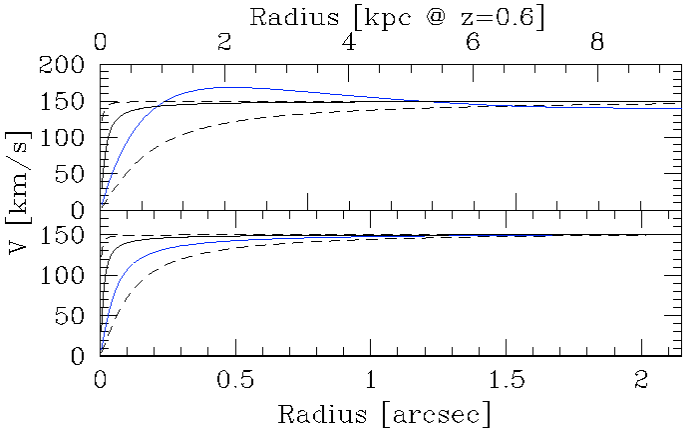

Fig. 1. Illustration of the $\Delta V_{\rm obs}$ correction method, for an early-type RC (*upper panel*, note that $V_{\rm max} > V_{\rm flat}$) and a late-type RC (*bottom panel*). The blue thick curves represent the input RC of the test, the black curves the best models (see text), and the dash-lines the two alternative RCs with non-optimal $r_{\rm t}$. We note that typical $r_{\rm t}$ values lead to velocity gradients on spatial scales that are much smaller than the typical seeing of ∼0.8 arcsec.

RC shape is a reasonable choice. The same shape was adopted in the local sample (see Sect. 2.2), which provided us with homogeneous estimates of the rotation velocity in both the local and distant samples. We chose not to fit a wide range of values for $r_{\rm t}$ because a visual inspection of VFs revealed that for almost all RDs, the gradient of the RC fell inside a single GIRAFFE IFU pixel (Flores et al. 2006 and Paper I). We therefore explored only three fixed values for $r_{\rm t}$ (see Fig. 1), which allowed us to investigate more extreme cases where the RC is relatively steep or, in contrast, relatively flat.

The arctan RC model cannot reproduce the central "bump" observed in some early-type galaxies (see, e.g., Fig. 1). Given the coarse spatial resolution of the GIRAFFE IFU (0.52 arcsec/pix, i.e., ∼3.5 kpc at $z = 0.6$) and the large size of the seeing disk compared to the typical scalelengths of distant galaxies, it might however be impossible to distinguish clearly between $V_{\rm max}$ or $V_{\rm flat}$ in distant galaxies. It might be expected that the asymptotic velocity V_0, corresponding to an arctan RC, is probably, in this case, an average value between $V_{\rm max}$ and $V_{\rm flat}$. Because we rely on $V_{\rm flat}$ as a kinematic measure of the rotation velocity in the local sample (see Sect. 2.2), we are naturally led to quantify all random and systematic uncertainties relative to $V_{\rm flat}$. Finally, we note that even for late-type RCs, $V_0 \sim V_{\rm flat}$ only if the RC has a well-defined plateau and if this plateau can be observed in terms of spatial coverage or *SNR*.

From each RC, a high-resolution data-cube was constructed, assuming a simple Gaussian shape for the emission line. For simplicity, we did not include noise in the simulations, assuming that the global uncertainty can be derived by estimating separately the influence of the noise and other effects (see Sect. 3.4). As a consequence, neglecting the doublet spectral nature of the [OII] emission line should not impact severally the results. The velocity width was assumed to be the minimal value observed in the σ-map, and the emission-line flux was taken from an exponential flux distribution, assuming $R_{\rm d} \sim R_{\rm half}/1.6$ (Persic & Salucci 1991) and limiting the spatial extent to a radius $2R_{\rm half} \sim 3R_{\rm d} \sim R_{\rm opt}$, where $R_{\rm d}$ is the disk scale-length, and $R_{\rm opt}$ is the optical radius. We chose to use $R_{\rm half}$ rather than direct $R_{\rm d}$ measurements because more than 80% of galaxies in the sample were not classified as simple spirals but had more complex morphologies (see Paper II), which could lead to meaningless $R_{\rm d}$ values. In contrast, $R_{\rm half}$ provides us with a uniform and well-defined size-parameter, which can be safely converted into $R_{\rm d}$ for thin exponential disks: using the bulge/disk decomposition of the RD subsample done in Paper II, we compared $R_{\rm d}$ with $R_{\rm half}/1.6$, and found a *maximal* difference of ∼ 0.1 arcsec, which is much smaller than the typical seeing during the observations (see also Puech et al. 2007a). Thus, such an error in $R_{\rm d}$ has little influence on the model, and we chose not to explore this parameter.

Each high-resolution data-cube was convolved by a 0.8 arcsec seeing, which corresponded to the median condition of the observations, and then rebinned to the GIRAFFE sampling, i.e., 0.52 arcsec/pix. From these simulated GIRAFFE data-cubes, simulated VFs and simulated $\Delta V_{\rm model}$ were derived as for real GIRAFFE data. We checked the influence of changing the seeing from 0.8 to 1.0 arcsec, on the $\Delta V_{\rm model}$: using Monte-Carlo simulations of 100 GIRAFFE data-cubes (see next section), we found a good linear correlation between the $\Delta V_{\rm model}$ obtained for a 1 arcsec seeing and that obtained for a 0.8 arcsec seeing, all other properties being equal. This fit indicated that for a 1 arcsec seeing, $\Delta V_{\rm model}$ was reduced by ∼0.05% compared to that obtained for a 0.8 arcsec seeing (see Fig. 2). Therefore, the maximal uncertainty on $\Delta V_{\rm model}$ due to seeing variations is ∼12 km s^{-1}, which corresponds roughly to the velocity spacing adopted for the searching grid used to correct $\Delta V_{\rm obs}$ (see above), which implies that this velocity grid was well adapted for our purpose.

To find the best model, we finally looked for the ($r_{\rm t}$,$V_{\rm flat}$) pair minimizing the difference between $\Delta V_{\rm model}$ and $\Delta V_{\rm obs}$. We checked that, in all simulations, such a criterion gives a unique

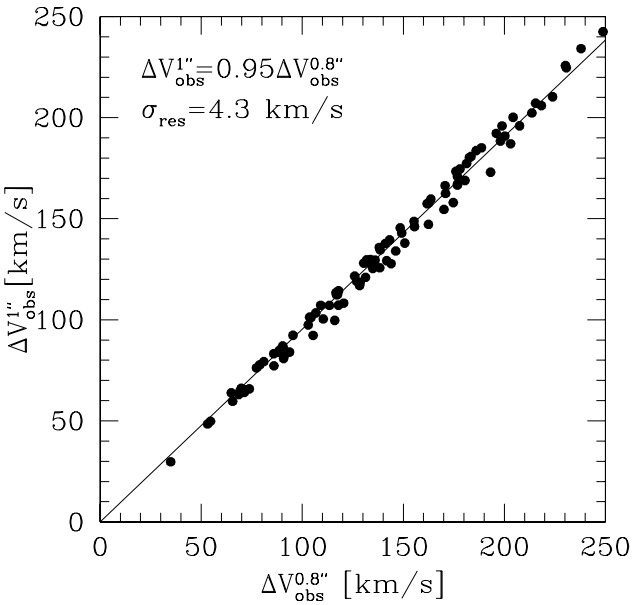

Fig. 2. Comparison between the $\Delta V_{\rm model}$ values obtained in Monte-Carlo simulations of 100 GIRAFFE data-cubes using a 0.8 and 1 arcsec seeing (see text). The black line is a linear fit fixing the intercept to zero. The residual dispersion is ~4.3 km s^{-1}.

solution. Results are listed in Table 1, and representative examples of this kinematical fitting for three RD galaxies are shown in Fig. 3.

3.2. Testing the method of correction

To test the correction method, we performed Monte-Carlo simulations of 100 GIRAFFE data-cubes. The parameter space investigated encompassed the inclination, half-light radius, PA, rotation velocity, and RC gradient, of values randomly chosen from the typical values observed for the GIRAFFE sample. Half of the Monte-Carlo simulations were generated using an arctan RC shape model, and the other half using an exponential term combined with a second-order polynomial term. This polynomial term allowed us to create a central velocity "bump" as observed in some early-type galaxies (see Fig. 1). We note, for late-type RCs, that the $V_{\rm flat}$ did not have to be located within the IFU, which allowed us to test how the correction procedure operated in this case. For early-type galaxies, $V_{\rm flat}$ should be located within the IFU, as $V_{\rm max}$ is generally located close to $2.2R_{\rm d} \sim 1.375R_{\rm half}$ (e.g., Courteau 1997), which almost always falls within the IFU (Flores et al. 2006). We note, however, that in some cases, because of the dynamical influence of the bulge, the RC of some early-type galaxies can show an extended velocity peak up to large distances (see, e.g., M 31, Carignan et al. 2006). The limited spatial coverage of the GIRAFFE IFU would probably provide us with an overestimation of the rotation velocity. In the RD sample, all galaxies besides one have $B/T < 0.2$, which means that such an effect cannot affect significantly the RD sample.

These simulated RCs were used to simulate GIRAFFE observations following the method outlined in Sect. 3.2. These simulated data-cubes were in turn used as inputs to test the method of correction on $\Delta V_{\rm obs}$. In Fig. 4, we compare the input rotation velocity $V_{\rm flat}$, with the asymptotic velocity V_0 of the best arctan model obtained using the method detailed above. We find a good linear correlation with $V_0 = [0.65 \pm 6.22] + [1.00 \pm 0.03]V_{\rm flat}$, consistent with $V_0 = V_{\rm flat}$, and a residual dispersion ~17 km s^{-1}. In this figure, we have distinguished between simulations where $V_{\rm flat}$ is sampled by the IFU (black circles) from those where this is not the case (black squares). If we compare the corrected velocity V_0 with the last point of the RC sampled by the IFU $V_{\rm end}$, both sets of simulations fall on the same region. In such a plot (not shown here), we find a similar result, with $V_0 = [-1.23 \pm 4.47] + [1.03 \pm 0.02]V_{\rm end}$, also consistent with $V_0 = V_{\rm end}$.

We checked that $r_{\rm t}$ had little influence on the $\Delta V_{\rm obs}$ correction by comparing the corrected rotation velocity, derived by allowing $r_{\rm t}$ to vary between the three values defined in Sect. 3.1, with that obtained by fixing $r_{\rm t}$ to the middle value of this grid, i.e. the one that makes most of the RC gradient fell inside one GIRAFFE pixel as observed in most cases. We found that both sets of values correlated well within ~6 km s^{-1} ($1-\sigma$), i.e., as expected, $r_{\rm t}$ has a negligible impact on the derived correction. This is due mainly to the large seeing size (~0.8 arcsec) compared to velocity gradients associated with typical $r_{\rm t}$ values (see Fig. 1), which significantly dilutes the variations of the RC gradient, once projected onto the IFU.

It is important to check whether or not these simulations are representative of real galaxies. To do this, we selected a few galaxies from the GHASP survey (Amram et al. 2002), which provides us with high spatial-resolution data-cubes for a morphologically-complete sample of local galaxies using Fabry-Perot interferometry. The analysis of the GHASP sample is still underway (Epinat et al. 2008), and a full comparison between local 3D data and distant 3D GIRAFFE data will be addressed in a future work. Here, we check whether or not the simulations are representative of local galaxies, especially in the range of velocity and size spanned by distant RDs. We restrict our choice to galaxies for which an arctan shape provides a relatively good representation of the RC, because we probe the accuracy of the correction applied to $\Delta V_{\rm obs}$, and not to the measurement itself, which is an independent issue. Given the limited number of galaxies meeting these criteria, we chose to restrict our choice to 7 such galaxies with rotation velocities ranging from 190 to 220 km s^{-1}, where are typical measurements for most distant RDs (see next Sect. 4). This choice allows us to sample roughly the most relevant velocity range for distant RDs, rather than testing a few isolated points spread over the full velocity range of the distant sample. We simulated GIRAFFE observations by degrading the Fabry-Perot high-resolution data-cube to the resolution of GIRAFFE observation (0.8 arcsec seeing) and then to the GIRAFFE IFU spatial sampling. From these data-cubes, we extracted a VF and $\Delta V_{\rm obs}$ as for real GIRAFFE data, and corrected them. These simulation results are shown as blue stars datapoints in Fig. 4, which agree with the Monte-Carlo simulations that fall in the same velocity range, reproducing the dispersion of the correlation. This confirms that we can confidently rely on the correction applied to $\Delta V_{\rm obs}$.

In Fig. 5, we plot all correction factors $\alpha = V_{\rm flat}/\Delta V_{\rm obs}$ obtained for the Monte-Carlo simulations. Both simulations of redshifted local galaxies and real GIRAFFE rotating disk galaxies fall in the same region of the plot, appart from three galaxies (J033212.39-274353.6, J033230.78-275455.0,J033245.11-274724.0), that show relatively large α. One is a compact galaxy (J033245.11-274724.0, see Paper II), while another one is seen almost edge-on (J033212.39-274353.6), which might explain the relatively high α. The last galaxy (J033230.78-275455.0) is a special case, because only half of the galaxy is detected in emission (this galaxy was shifted into the RD+ class in Sect. 2.1). We checked that the results presented in this paper are not

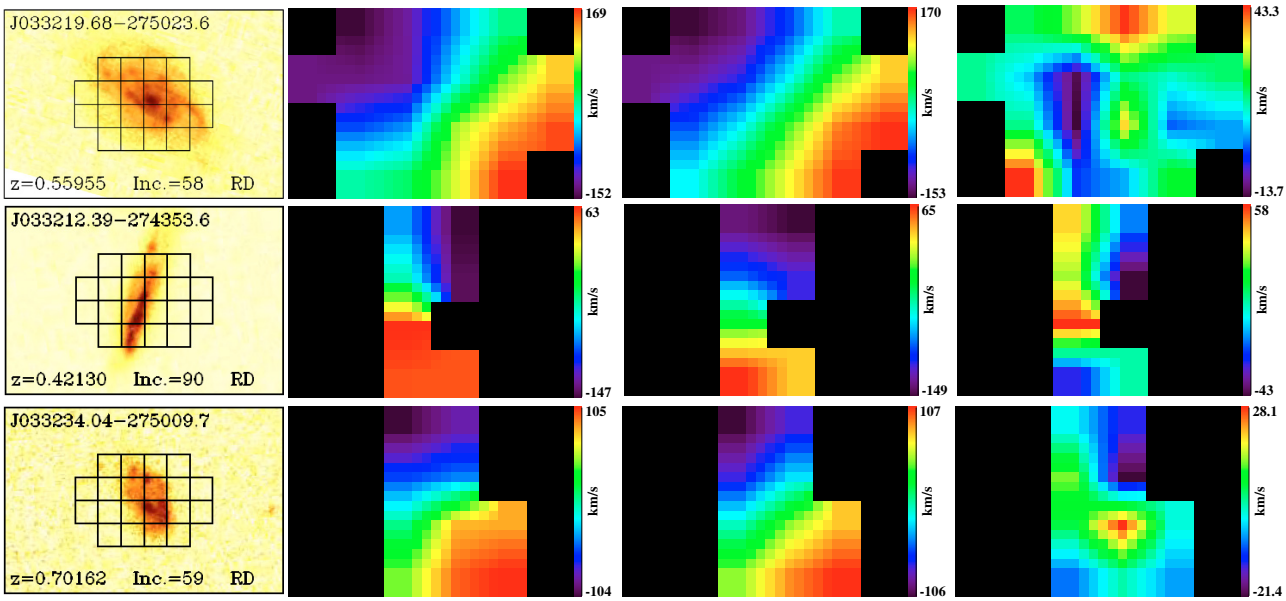

Fig. 3. Examples of kinematical fitting of three $z \sim 0.6$ RD galaxies. *From left to right*: HST/ACS F775W image with the GIRAFFE IFU superimposed (from Paper I), observed VF (shown with a 5×5 interpolation see Paper I), best modeled VF (shown with a 5×5 interpolation), residual map between the observed and modeled VFs. Relatively large differences are found only close to the minor axis, where departure from pure circular motion is artificially exaggerated by projection effects (see a discussion of this effect in, e.g., Chemin et al. 2006).

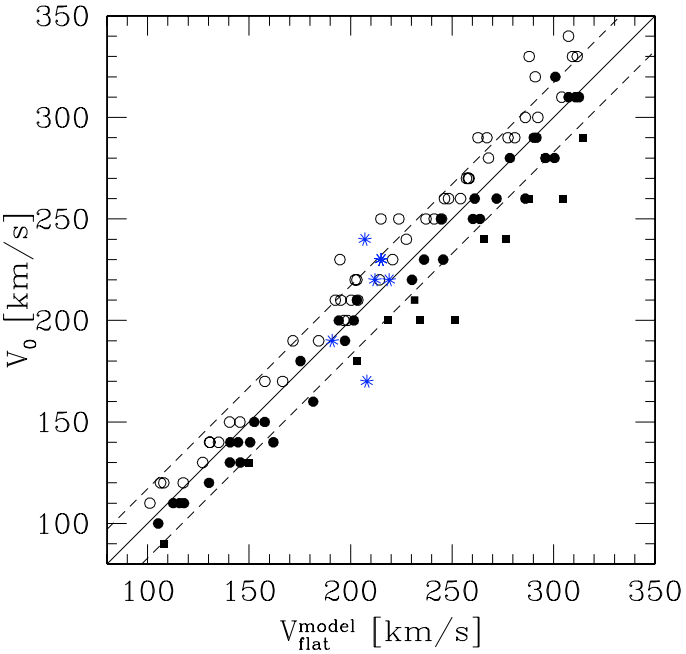

Fig. 4. Comparison between the $V_{\rm flat}$ used as inputs to the Monte-Carlo simulations of 100 GIRAFFE data-cubes, with the V_0 values obtained after using the method of correction described in Sect. 3.2. Black dots represent RCs generated using an arctan model (i.e., late-type like RCs), while open circles represent RCs typical of early-type galaxies. Black squares represent simulations where the rotation velocity is not sampled by the IFU (see text). The black line is a linear fit, and the dash lines represent the $1-\sigma$ residual dispersion $\sim$17 km s^{-1}. Blue stars represent real observations of local galaxies artificially redshifted to $z \sim 0.6$ (see text).

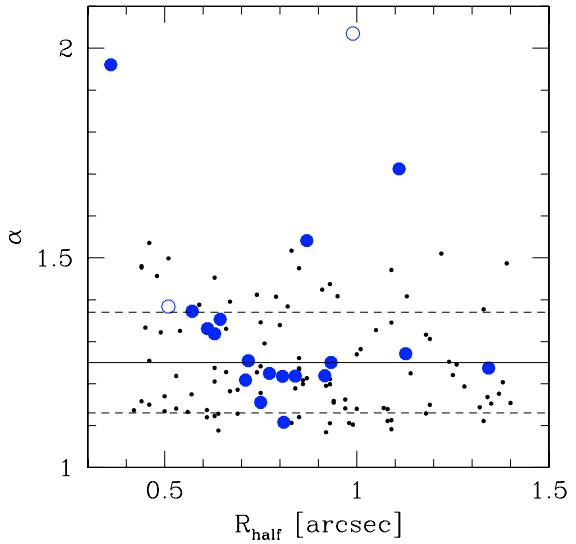

Fig. 5. Correction factors α used to correct $\Delta V_{\rm obs}$ for RDs (blue dots; open blue dots represent the two RD+ galaxies). Small black dots correspond to Monte-Carlo simulations of 100 GIRAFFE data-cubes in the same range of half-light radius, PA, inclination, rotation velocity, and RC gradient (see text). The horizontal dash line represents to the mean correcting factor of 1.25 derived from Monte-Carlo simulations, while the $1-\sigma$ dispersion around the mean is shown in dash lines.

significantly affected when these three special objects are removed from the sample. In the RD subsample, we found a median $\alpha \sim 1.26$, consistent with what is found in the Monte-Carlo simulations, with a mean $\alpha = 1.25 \pm 0.12$.

3.3. Random uncertainty budget of the rotation velocity derivation

The uncertainty budget can be decomposed into uncertainties related to $\Delta V_{\rm obs}$, and those related to the correction applied to $\Delta V_{\rm obs}$ to obtain $V_{\rm flat}$.

The main source of uncertainty that can affect $\Delta V_{\rm obs}$ is that associated with a finite spectroscopic *SNR* in the measurement of $V_{\rm max}^{\rm IFU}$ and $V_{\rm min}^{\rm IFU}$, which can be quantified using Monte-Carlo simulations (see Fig. 6). For each galaxy, we used the *SNR* maps derived in Paper I to estimate the mean *SNR* uncertainty on $V_{\rm max}^{\rm IFU}$

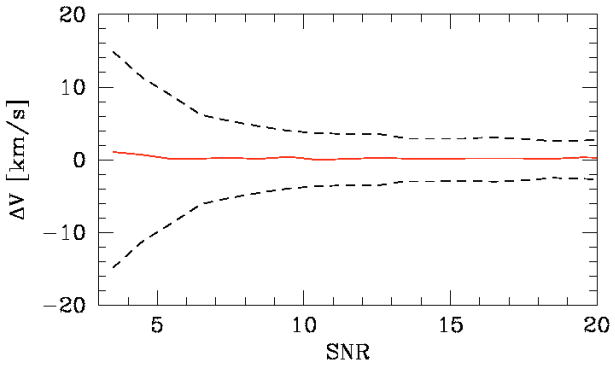

Fig. 6. Monte-Carlo simulations of the velocity measurement accuracy (see Paper I, for details). The red line shows the corresponding bias (almost zero), while the black dashed lines shows the $1-\sigma$ error: $\sim$12 km s^{-1} between $SNR = 3-5$, $\sim$5 km s^{-1} between $SNR = 5-10$, and $\leq$2 for $SNR \geq 10$.

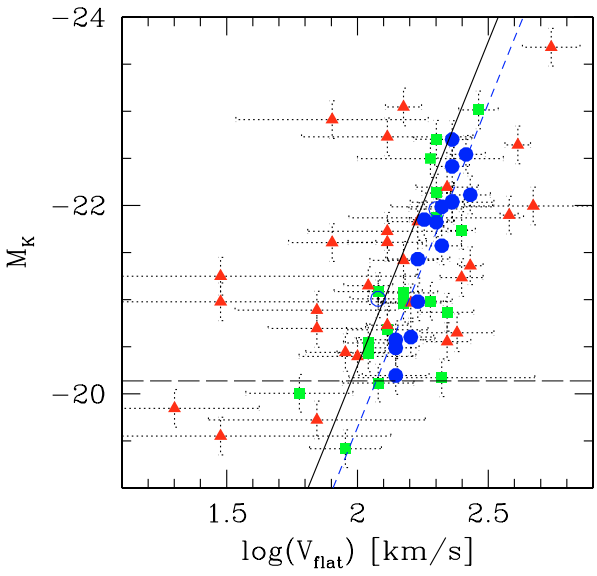

Fig. 7. Evolution of the K-band TFR (AB magnitudes). The completude limit $M_K \sim -20.14$ (corresponding to $M_J = -20.3$, see Sect. 2) is indicated by an horizontal dash line. Blue dots represent RDs (the two RD+ galaxies are represented with open blue dots), green squares PRs, and red triangles CK galaxies. The black line is the local TFR, while the blue dash-line represent a linear fit to the $z \sim 0.6$ TFR (see text).

and $V_{\rm min}^{\rm IFU}$, i.e., on $\Delta V_{\rm obs}$. We found a median (mean) uncertainty due to a finite SNR of $\sim$9 km s^{-1} (8 km s^{-1}).

We used Fig. 4 to quantify the uncertainty associated with the correction made to $\Delta V_{\rm obs}$. We found 17 km s^{-1} ($1-\sigma$ residual dispersion), with no noticeable systematic uncertainties. We note that this uncertainty takes into account cases where the RC is not fully sampled by the IFU. As we have already pointed out, one galaxy in the sample deserves more consideration. Only part of the galaxy J033230.78-275455.0, which was classified as RD+ (see Sect. 2.1), was detected in emission (see Paper I). $\Delta V_{\rm obs}$ does not encompass a symmetric range along the RC, which biases the rotation-velocity input of the model to a lower value. Considering a rough RC model, composed of a first, linear, rising part up to $R_{\rm max} = 2.2R_{\rm D}$ (Persic & Salucci 1991), and a second flat part, we estimate a $\sim$30 km s^{-1} correction to "symmetrize" $\Delta V_{\rm obs}$. This correction is convolved directly by the other uncertainty factors on $\Delta V_{\rm obs}$. Following Sects. 3.1 and 3.2, we also took into account uncertainties due to seeing and $r_{\rm t}$ variations ($\sim$5 and 6 km s^{-1}, respectively), which produced a total uncertainty for the correction on $\Delta V_{\rm obs}$ of $\sim$19 km s^{-1}.

The total uncertainty on $V_{\rm flat} \times \sin(i)$ (i.e., the radial rotation velocity uncorrected for inclination) was derived by adding in quadrature all the previous terms. We finally propagate the uncertainty associated with the inclination, which is $\pm$5 degrees, according to Paper I. We finally found a median (mean) total uncertainty on $V_{\rm flat}$ of $\sim$37 km s^{-1} (44 km s^{-1}). The $1-\sigma$ dispersion of the total uncertainties around the mean is $\sim$30 km s^{-1}.

4. The *K*-band Tully-Fisher relation at $z \sim 0.6$

4.1. Results

We compare both the distant and local K-band TFR in Fig. 7. Holding the slope to the local value, $\sigma_{\rm res}$ increases from RDs (0.31 mag), to PRs (0.80 mag), and CKs (2.08 mag). Restricting the distant TFR to dynamically well-relaxed RDs, the local and distant relations have comparable $\sigma_{\rm res}$: we therefore confirm quantitatively the previous findings of Flores et al. (2006) that all of the enlarged dispersion of the distant TFR comes from non-relaxed galaxies. If we allow the slope to vary during the fit, we find a residual dispersion of 0.31 mag. This indicates that assuming no evolution in slope appears to be a reasonable assumption.

The zero point of the TFR of distant RD galaxies is found to be -5.88 ± 0.09 ($1-\sigma$ bootstrapped error, slope fixed), i.e., 0.66 mag fainter that the local zero point. Allowing the slope to vary during the fit, we find a zero point of -5.07 ± 2.37 and a slope of -7.24 ± 1.04 in agreement (within the corresponding uncertainties) with those derived by fixing the slope to the local value. This strongly suggests no evolution in slope of the K-band TFR. Given the limited number of RDs in the distant sample (16), we adopt the zero-point value derived by keeping the slope to the local value. We note that if we consider the RD+ class (18 galaxies, see Sect. 2), we find similar results (see Table 2).

Table 2. Fits to the local and distant K-band TFRs, using $M_K(\rm AB) = a + b \times \log(V_{\rm flat})$.

K-band TFR	Slope a	Zero point b	Comments
Local relation	-6.88 ± 0.57	-6.54 ± 1.33	SDSS subsample
Distant RDs	-6.88	-5.88 ± 0.09	Using local slope
Distant RDs	-7.24 ± 1.04	-5.07 ± 2.37	Slope free
Distant RD/RD+	-6.88	-5.92 ± 0.10	Using local slope
Distant RD/RD+	-6.47 ± 1.30	-6.85 ± 2.98	Slope free

We find in the distribution of M_K residuals, a skewness and a kurtosis of -0.22 and -0.99, respectively for RDs: this is roughly consistent with the Gaussian residuals, within the $1-\sigma$ expected thresholds[2]. This indicates that residuals are not biased significantly on any side of the relation. A Welcher's t-test then provides a probability $\ll$1% that the local and distant relations have the same zero point. We note that during the fitting procedure, we weighted all the rotation velocities by their associated uncertainties. Therefore, the result of the Welcher's t-test means that within random uncertainties, the zero-point difference of 0.66 mag between the distant and the local relations is statistically significant.

[2] For a distribution of n points, these thresholds are $\sqrt{(6/n)}$ and $\sqrt{(21/n)}$ respectively ($n = 16$ is the present case).

4.2. Systematic uncertainty budget

We investigate which systematic effects could bias the evolution of TFR zero point detected between $z \sim 0.6$ and $z = 0$.

4.2.1. Photometric systematic uncertainty

As stated in Sect. 2, we do not expect any noticeable systematic-effect on measurements due to photometric measurement or calibration. However, one possible exception is the extinction correction made on both local and distant galaxies. Even if we follow exactly the same procedure for the two samples, one might wonder whether or not the low surface-brightness outer-regions in distant galaxies could be far less well detected compared to local galaxies, which would create a bias in the derivation of their axis ratios and extinction corrections. However, we found in Paper II that the HST/ACS imaging used to derive the axis ratio in distant galaxies allows us to reach the optical radius ($\sim 3.2 \times R_{\rm d}$), which limits such a bias. We note that extinction corrections are relatively small in the K-band: in the distant sample, we find a mean/median correction of 0.11 ± 0.05 mag ($1-\sigma$ dispersion), while in the local sample, the mean (median) correction is found to be $0.15(0.14) \pm 0.05$, which are consistent within the respective uncertainties.

4.2.2. Effects related to the comparison to the local relation

One important aspect about the evolution of the TFR is to control systematic effects between the distant and local relations. These considerations have led us to adopt as a local reference the TFR derived by Hammer et al. (2007) for a complete subsample of the SDSS (Pizagno et al. 2007, see Sect. 2.2). However, there are several differences between the local and distant samples that could lead to possible biases when comparing the corresponding TFRs.

First, kinematical data are obtained using different techniques (3D spectroscopy vs. long-slit spectroscopy). We mitigated this effect by restricting the local sample to galaxies having a well-defined RC (see details in Hammer et al. 2007). This also mitigates the assumption that both local and distant galaxies have RC shapes than can be well described by an arctan (see Sects. 2.2 and 3.2). Second, a different emission line is used for deriving the rotation velocity ([OII] and H_α). However, both emission lines are found to provide similar estimates of the rotation velocity (e.g., Saintonge 2007). Third, in the local sample, V_{80} (defined as the velocity at a radius that encompasses 80% of the light) is used as a proxy for $V_{\rm flat}$, while we directly used the asymptotic V_0 from the arctan RC in the distant sample. V_{80} is a reliable proxy for $V_{\rm flat}$, as shown in Hammer et al. (2007) (see also Pizagno et al. 2007). Finally, one possible caveat about the use of 2MASS K-band magnitudes was recently pointed out by Noordermeer & Verheijen (2007), i.e. that 2MASS underestimates the K-band luminosity in relatively low surface brightness galaxies. We note that this bias would go in the opposite trend compared to the evolution seen in the TFRs, i.e., to shift the local relations towards brighter magnitudes or larger stellar masses. However, we have also mitigated this effect by restricting the local relation to galaxies having $\mathrm{Log}(V_{\rm flat}) \geq 2.2$, i.e. to the most massive galaxies (see Sect. 2.2).

4.2.3. Kinematic systematic uncertainty

We restricted the analysis of the TFR evolution to well-relaxed RDs. In distant TFR studies, it is often assumed that the (gas) rotation velocity can be simply derived as the half-amplitude of the VF divided by $\sin(i)$ (modulo spatial-resolution effects): an important assumption behind this simple prescription is that the azimuthal velocity component of the 3D velocity vector within the galaxy (i.e., the rotation) dominates its projection along the line-of-sight. This assumption should always be checked a posteriori, by showing that residuals between a rotating-disk model and the observed VF are small compared to the amplitude of rotation motions. In the case of GIRAFFE RDs, there are few doubts that this assumption is correct, because their modeled VFs match the observed ones (see Paper I).

Conversely, CK galaxies are clearly out of dynamical equilibrium (see Flores et al. 2006 and Paper I). As a consequence, one does no longer know which component of the 3D velocity vector dominates its projection along the line-of-sight. If these galaxies are associated with mergers, as we will discuss below, deriving the rotation velocity in this way is probably uncertain, if not meaningless. This is the reason why in this study, we restricted the analysis of the TFR to well-relaxed RDs.

In Sect. 3, we tested extensively the method of correction used to correct $\Delta V_{\rm obs}$ for spatial-resolution effects. All galaxies were assumed to be RDs, regardless of their kinematical class (see Puech et al. 2006a, 2007a). However, this provides uniform α values that are independent of kinematical class: a misclassification of a galaxy has no impact on the way α is derived. This approach helps to compare with long-slit spectroscopy results, where all galaxies are implicitly assumed to be RDs (e.g., Conselice et al. 2005). As explained above, the fit to the TFR is restricted to RDs only, and therefore this cannot affect the evolution of the zero point of the TFR.

One might wonder whether or not the slight bias found in Fig. 4 between early- and late-type galaxies could influence significantly the results. Once translated into $\log(V_{\rm flat})$ (using Eq. (1)), the offset of the distant TFR is found to be -0.1 dex between $z \sim 0.6$ and $z = 0$, which is much larger than that found in Fig. 4 for early-type galaxies ($\sim$0.025 dex). Late-type galaxies have the opposite trend, which provides a -0.014 dex offset in Fig. 4. It is impossible to explain all of the shift in the distant TFR zero point in terms of such a morphological bias. Looking at the TFR residuals against B/T for RDs analyzed in Paper II, we find no special trend, which excludes the presence of a bias.

Another source of systematic uncertainty could be the limited spatial coverage of the GIRAFFE IFU. Figure 4 (see the black squares) shows that when the plateau of the RC is not sampled by the IFU, the recovered rotation velocity is underestimated on average by $\sim$0.03 dex. We note that this effect generally leads to the underestimation of $V_{\rm flat}$, which would increase the shift of the zero point between the local and the distant TFRs. However, most of the RDs are well spatially covered by the IFU (see Flores et al. 2006 and Paper I), and this could affect a few galaxies in our sample. It is thus unlikely that such an effect could affect significantly the results in a systematic way.

Finally, the most important possible systematic uncertainty likely comes from our limited knowledge of the seeing during observations. Individual variations from galaxy to galaxy leads to relatively small random uncertainties (see Sect. 3.2). However, we assumed a uniform value of 0.8 arcsec during the rotation-velocity correction process. According to Fig. 2, changing the seeing in the simulations from 0.8 to 1.0 arcsec implies a systematic effect of -0.02 dex on the rotation velocity correction.

4.2.4. Total systematic uncertainty

The only possible systematic effect we can identify so far is that associated with the kinematics, due to the correction for the rotation velocity. Using Eq. (1), this translates into a possible systematic uncertainty of ±0.14 mag in the 0.66 mag evolution of the K-band TFR zero point between $z \sim 0.6$ and $z = 0$, which represents 20% of the shift.

5. Discussion

5.1. Comparison with Flores et al. (2006)

In Flores et al. (2006; see also Puech et al. 2007a), we used hydro-dynamical simulations of an Sbc galaxy to infer a mean correction factor $\alpha = 1.2 \pm 0.05$ on $V_{\rm max}$ for galaxies of typical diameters between 2 and 3 arcsec: this value is less than that found here using Monte-Carlo simulations. At first sight, it is surprising to find a larger mean α for $V_{\rm flat}$ than for $V_{\rm max}$ (since $V_{\rm flat} \leq V_{\rm max}$). The explanation is likely linked to the fact that in Flores et al. (2006), we did not consider all possible ranges of size, PA, inclination, rotation velocity and RC gradient to derive this mean correction, because we were limited by the hydro-dynamical models of spiral galaxies available to us at that time. Another difference is the exponential dependence of α with galaxy size found in Flores et al. (2006), which is not reproduced here. The reason for this is that in Flores et al. (2006), we used the same simulation of an Sbc galaxy to simulate distant galaxies of different sizes, which induced an intrinsic correlation between the RC gradient and the galaxy size. Our tests show that if we introduce this correlation in the Monte-Carlo simulations, we then recover the exponential variation of α with $R_{\rm half}$.

The brightening found in the K-band TFR was not initially detected by Flores et al. (2006). In Fig. 8, we show the K-band TFR obtained following the Flores et al. (2006) method to correct $\Delta V_{\rm obs}$, i.e., applying a constant correction factor of 1.2. The black line shows the Verheijen (2001) K-band local TFR using $V_{\rm flat}$ as a kinematical tracer for the rotation velocity, i.e., the relation used as a local reference by Flores et al. (2006). Both the local and distant relation are then in good agreement: if we fix the slope of the distant relation to the local one, we find a shift ~0.1 mag between the zero point of the distant and the local relations. Therefore, we retrieve the Flores et al. (2006) results that no significant evolution in zero point can be detected. The reason for such a difference is twofold.

First, as detailed in Hammer et al. (2007), we found a discrepancy between the K-band TFR derived in the Verheijen (2001) sample, compared to those derived in two other local samples (Courteau 1997; Pizagno et al. 2007). We show in Hammer et al. (2007) that this discrepancy is due to the larger fraction of faint and slow rotating galaxies in the Verheijen (2001) sample compared to the two other ones. Such galaxies have a larger gas fraction, which results in a different slope at the low-mass end of the TFR (McGaugh 2005). Noordermeer & Verheijen (2007) derived a new K-band local TFR: they found a slope similar to the one inferred by Hammer et al. (2007) after restricting the Verheijen (2001) TFR to the high-mass end. In Flores et al. (2006), the relation used as a local reference was however the Verheijen (2001) relation. If we refit the distant RD subsample using the rotation velocities derived following Flores et al. (2006), but using the slope of the SDSS local relation (i.e., the one used in Fig. 7, see the blue lines in Fig. 8), we find a shift ~0.4 mag between the distant and the local zero points. Compared to Flores et al. (2006), we use a different local sample, which provides a better control of systematic effects

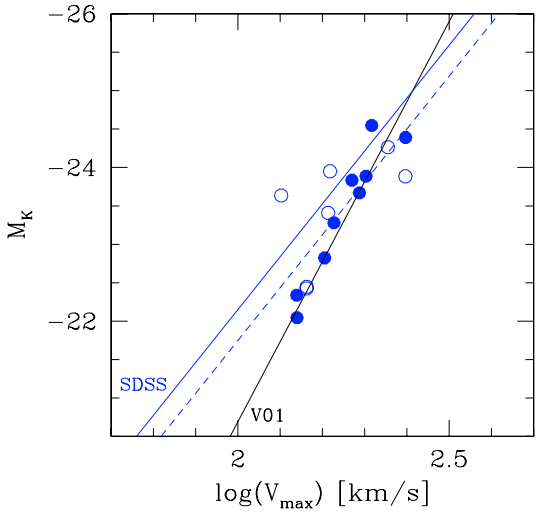

Fig. 8. K-band TFR derived following the Flores et al. (2006) methodology, for the RD subsample. The black line is the local relation of Verheijen (2001), i.e., the one used as a reference by Flores et al. (2006). Note that K-band magnitudes in the distant sample have been converted into the Vega system using M_K(Vega) = M_K(AB) − 1.85. For simplicity, we assume that the K' magnitudes of Verheijen (2001) are roughly equivalent to those derived in the distant sample using the ISAAC Ks filter. The blue line is the SDSS local TFR used as a reference in this study (converted into the Vega system). The blue dash line is a linear fit to the distant RDs, which has a zero point 0.4 mag lower than the local one, fixing the slope to the local value. Open symbols represent galaxies from the new CDFS sample, while full symbols represent galaxies used in Flores et al. (2006).

that can occur in the comparison with the distant sample (see Sect. 4.2.2): this rigorous approach allows us to explain ~60% of the TFR zero-point shift, previously hidden by spurious effects.

Second, we have significantly improved the method for correcting the rotation velocity since the preliminary work of Flores et al. (2006). This is illustrated in Fig. 9, where we compare the rotation velocities derived following Flores et al. (2006) and those derived in this study: this figure reveals that Flores et al. (2006) underestimated the rotation velocity in RDs by 11% on average, which corresponds to a ~0.05 dex shift in $\log(V_{\rm flat})$, or ~0.3 mag once converted into a M_K shift using Eq. (1). Therefore, we attribute the remaining ~40% of shift in the TFR zero point, previously undetected, to the improvement in the rotation-velocity derivation.

Finally, Fig. 8 provides us with a useful cross-check of the new method used in this study to correct the rotation velocity. In Fig. 8, one RD galaxy (J033212.39-274353.6) appears to be shifted to lower velocities compared to other distant rotating disks. This galaxy was identified as having a particularly high α value in Sect. 3.3, while its data are well described by the TFR in Fig. 7. This suggests that the new method of correction appears to be better suited for deriving rotation velocities: comparing Fig. 8 with 7, we note that the dispersion of the RD subsample is significantly reduced using the new method of correction.

5.2. Origin of the scatter in the distant relation

Using the spatially-resolved kinematics provided by 3D spectroscopy, we confirm earlier results that the dispersion of the distant relations can be explained by the presence of dynamically non-relaxed galaxies (Flores et al. 2006). These galaxies are found to be out of dynamical equilibrium, with random

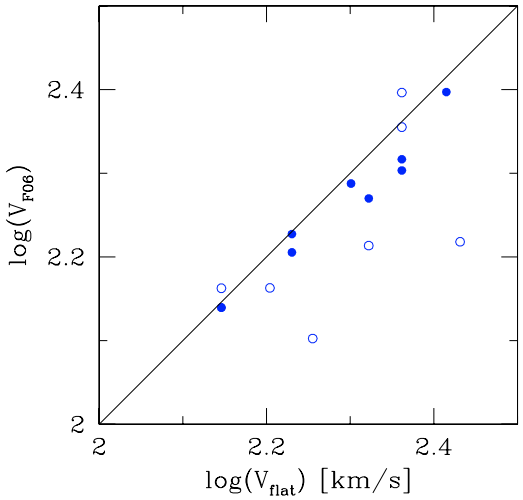

Fig. 9. Comparison between the rotation velocities V_{F06} obtained using the method of Flores et al. (2006) (i.e., a constant correction factor of 1.2) vs. rotation velocities $V_{\rm flat}$ derived using the new method used in this paper, for the subsample of RDs. V_{F06} underestimates $V_{\rm flat}$ by ∼11% on average. Open symbols represent galaxies from the new CDFS sample, while full symbols represent galaxies used in Flores et al. (2006).

motions instead of ordered motions, especially for the most compact galaxies (Puech et al. 2006a; Weiner et al. 2006). Ongoing comparisons between hydrodynamical simulations of galaxy mergers with GIRAFFE data reveal that they could be associated with major mergers (Puech et al. 2007a; Puech et al., in prep.). Such events provide a natural link between CK galaxies and morphologically-peculiar galaxies (see Paper II), which causes an increase in the dispersion of the TFR at high redshift (Kassin et al. 2007; Atkinson et al. 2007).

On the other hand, it is still unclear whether or not more quiescent processes, such as secular gas accretion through internal processes (bars), or cold-gas flows (Dekel & Birnboim 2006; Keres et al. 2005), could explain such anomalous kinematics on a relatively large spatial scales, especially for CK galaxies (see Paper I). More work is required to compare dynamical predictions of such events with observations.

5.3. Comparison with the evolution of the K-band luminosity density

Finding a 0.66 mag *brightening* of the K-band TFR between $z \sim 0.6$ and $z = 0$ appears to be quite surprising, given the opposite trend seen in the evolution of the K-band luminosity density in "blue" galaxies over the same redshift range. One may reasonably assume that "blue" star-forming galaxies and emission-line galaxies belong to the same population (Hammer et al. 1997): Arnouts et al. (2007) find that the K-band luminosity density of blue star-forming galaxies *fades* by 0.5−0.6 mag from $z \sim 0.6$ to $z = 0$, which is exactly the opposite trend. What appears to be a clear contradiction simply reflects two different methodologies.

As we have detailed above, the TFR allows us to compare two physically-connected populations of galaxies, i.e., the local spirals and the distant rotating disks: the evolution of this relation directly reflects the evolution of the K-band luminosity in *rotating disks of similar total mass* between $z \sim 0.6$ and $z = 0$, assuming that the rotation velocity can be used as a proxy for the total mass (Hammer et al. 2007). On the other hand, the color selection used to select "blue" galaxies at $z = 0$ and at $z \sim 0.6$ can produce heterogeneous galaxy populations, as noticeable when comparing their luminosity densities. Optical colors are well known to be seriously affected by instantaneous star formation and extinction. The evolution of the K-band luminosity density in "blue" galaxies reflects the number evolution of "blue" galaxies, which are much more numerous at high redshift (e.g., Ellis 1997).

To check that there is no contradiction between the evolution of the TFR zero point and the evolution of the K-band luminosity density, we derived the K-band luminosity density in the complete GIRAFFE sample, i.e., including all dynamical classes. As stated in Sect. 2.1, the GIRAFFE sample is representative of $z \sim 0.6$ emission-line galaxies with $M_J(\mathrm{AB}) \leq -20.3$ (i.e., with $M_{\rm stellar} \geq 1.5 \times 10^{10}\ M_\odot$, see Paper I). We therefore expect a K-band luminosity density in this sample that represents the luminosity density of "blue" galaxies at these redshifts. We estimated the K-band luminosity in the GIRAFFE sample to be $\log(\rho_K) = 8.74\ L_\odot\,\mathrm{Mpc}^{-3}$, which agree well with the K-band luminosity density of "blue" star-forming galaxies found by Arnouts et al. (2007). This comparison confirms that the GIRAFFE sample is representative of $z \sim 0.6$ emission-line galaxies: the K-band luminosity density in the GIRAFFE sample is consistent with the results inferred from studies using far larger samples.

5.4. Did distant rotating disks double their stellar-mass over the last 6 Gyr?

Once restricted to well-relaxed RDs, we find, between $z \sim 0.6$ and $z = 0$, a shift in the TFR zero point of 0.66 ± 0.14 mag in M_K, or -0.1 ± 0.02 dex in $\log(V_{\rm flat})$. We consider the interpretation of this shift in terms of galaxy evolution.

Could there be any so-called "progenitor bias" between distant RDs and local relaxed spirals, which could imply that the latter would not be the descendants of the former? Local RDs are found to be twice as numerous as distant ones (see Paper II), which implies that some were not in a relaxed dynamical state at $z \sim 0.6$ (being then PR or CK). However, local intermediate-mass spirals have only a low probability to have undergone a major merger since $z \sim 0.6$ (15−30%, as discussed in Puech et al. 2007a): this means that most distant RDs must dynamically evolve smoothly towards local relaxed spirals, which implies that distant RDs are the progenitors of a majority of local spirals. Therefore, it makes sense to interpret the evolution of the RD-restricted TFR as an evolution in luminosity, rotation velocity, or a combination of the two. We reiterate that we assume no evolution in slope (see Sect. 4.1): a larger sample would be required to tackle directly the possible evolution in slope of the TFR and determine the details of the evolutionary path between distant and local RDs.

We discuss the possibility that this shift could correspond to a pure luminosity brightening of 0.66 ± 0.14 mag in RDs over the past 6 Gyr. Such a luminosity-brightening in RDs would correspond to a growth in stellar-mass, which can be estimated in the following way. Between $z \sim 0.6$ and $z = 0$, the evolution in $\log(M_{\rm stellar}/L_K)$ is found to range between 0.13 and 0.16 dex (Drory et al. 2004; Arnouts et al. 2007), depending on the selection criteria. Using $\log(M_{\rm stellar}) = \log(M_{\rm stellar}/L_K) + \log(L_K)$, one finally finds a stellar-mass evolution of 0.39−0.42 dex. A more exhaustive derivation, using the stellar-mass TFR, leads to a similar conclusion, with an evolution in zero point of $0.36^{0.21}_{-0.06}$ dex between $z \sim 0.6$ and $z = 0$ (see Appendix A). On the other hand, the evolution of the cosmic stellar-mass density over the same redshift range is found to be ∼0.1−0.16 dex (Dickinson et al. 2003; Drory et al. 2004; Arnouts et al. 2007).

Hammer et al. (2005) found that most of the present-day stellar-mass formed since $z = 1$ occur in intermediate-mass galaxies (see also Bell et al. 2005), which include 60% of emission-line galaxies at $z \sim 0.6$ (Hammer et al. 1997). Hence, if we assume that, on average, quiescent galaxies do not evolve in stellar-mass, one can estimate the growth in stellar-mass between $z \sim 0.6$ and $z = 0$ in intermediate-mass, emission-line galaxies to be ~0.32−0.38 dex. Therefore, this interpretation of the TFR zero-point shift as a pure luminosity evolution is roughly in agreement with the evolution of the cosmic stellar-mass density over the same redshift range. This interpretation is supported by the fact that distant RDs are found to be LIRGs or at least star-bursting, i.e., they are actively forming stars at very high rates (see Paper II).

Interpreted in this way, the evolution of the zero point of the K-band TFR reflects the growth in stellar-mass of the most active population over the past 6 Gyr, i.e. star-forming intermediate-mass galaxies, by a factor ~2.5−2.6. This compares well with the gaseous O/H phase abundance of $z \sim 0.6$ emission-line galaxies, which is, on average, half that of present-day spirals for a similar range of stellar mass (Liang et al. 2006). Such an evolution in stellar mass would imply that RDs converted an important amount of gas into stars over the past 6 Gyr. In other words, the main evolutionary path for RDs during the past 6 Gyr would be conversion of gas into star through gas supply, which is further supported by their relatively low gas-disk V/σ values (Puech et al. 2007a) and the inside-out build-up of their stellar disks (see a detailed discussion in Paper II).

The opposite interpretation is that the shift in the zero point of the K-band TFR corresponds to a pure rotation-velocity evolution of -0.1 ± 0.02 dex between $z \sim 0.6$ and $z = 0$. Even in this case, the observed evolution in $M_{\rm stellar}/L_K$ over this redshift range still implies, on average, a substantial growth in stellar mass of 0.13−0.16 dex in intermediate-mass galaxies (see above). As a consequence, the stellar mass growth in *quiescent* intermediate-mass galaxies should be approximately similar because the stellar mass growth in the entire population (i.e., quiescent or not) is observed to be similar in this redshift range. This is clearly not what is observed, because ~80% of the stellar mass formed since $z = 1$ occurred in star-forming galaxies (LIRGs, see Hammer et al. 2005). We can therefore rule out a pure evolution along the velocity axis.

The last possibility is a combined evolution along both axes, i.e. a simultaneous brightening in luminosity with a decrease in rotation velocity $V_{\rm rot}$. According to the Virial theorem, $V^2_{\rm rot}$ scales as the ratio of the total mass enclosed within the optical radius $R_{\rm opt}$, over $R_{\rm opt}$ (~$3.2R_{\rm d}$ in both distant and local galaxies, see Paper II). A decrease in $V_{\rm rot}$ between $z \sim 0.6$ and $z = 0$ would then imply a decrease in this ratio, which in turn would imply that $R_{\rm opt}$ (or $R_{\rm d}$) increases faster than the total mass over the same redshift range. Between $z \sim 0.6$ and $z = 0$, $R_{\rm d}$ does not seem to evolve strongly, at least in the RD subsample (see Paper II; see also Puech et al. 2007a). Therefore, only a moderate increase in the total mass enclosed within $R_{\rm opt}$ could occur over this redshift range. Such a scenario would agree with observations: as stated above, local intermediate-mass spirals have a low probability to have undergone a major merger since $z \sim 0.6$ (15−30%, see Puech et al. 2007a, and references therein). Therefore, most distant RDs should be already mostly assembled at $z \sim 0.6$, and should not undergo strong evolution in terms of total-mass from $z \sim 0.6$ to $z = 0$.

To explore the real evolution along both axes, we compare our results with the model of spherical gas accretion of Birnboim et al. (2007). Birnboim et al. (2007) present a model of accretion for a star-bursting galaxy at $z \sim 0.7$ and describe its subsequent evolution in terms of mass, down to $z = 0$. Although it is not clear whether or not such a model could be representative of all properties of distant RDs, we assume that it can be used to constrain the average mass evolution in a typical RD halo. In that case, the results of Birnboim et al. (2007) would suggest that the baryonic mass in the disk remains constant between $z \sim 0.6$ and $z = 0$, while the *Virial* baryonic mass roughly doubles (see their Fig. 2). On the other hand, Conroy et al. (2007) found that the Virial-to-stellar mass ratio in intermediate-mass galaxies is roughly constant between $z = 1$ and $z = 0$. Assuming that the subsample of RDs follows the same trend, one can combine the Conroy et al. (2007) observational results with the model of Birnboim et al. (2007), and find that RDs would roughly double their stellar-mass between $z \sim 0.6$ and $z = 0$. Accounting for the evolution in mass-to-light ratio over this redshift range, this would translate into an evolution of 0.35−0.43 mag in luminosity, to be compared with the 0.66 mag found in the evolution of the TFR zero point. Once translated into $\log(V_{\rm flat})$, this would allow a −0.04 dex evolution along the velocity axis, between $z \sim 0.6$ and $z = 0$.

In conclusion, we find that the most likely interpretation of the evolution of the TFR zero point is the one in which this shift reflects mostly a luminosity evolution of RDs. We estimated an upper limit to the contribution of an evolution along the velocity axis to be at most one half of the total shift of zero point. Such a brightening of distant RDs over the past 6 Gyr would indicate a doubling of their stellar-mass, which is independently supported by their other dynamical and morphological properties.

Finally, this could suggest that the *baryonic* (stars *plus* gas) TFR would not evolve with redshift: if one accounts for the (average) two times larger gas fraction of $z \sim 0.6$ galaxies compared to $z = 0$ (Liang et al. 2006), one finds that distant galaxies roughly fall back onto the local smTFR (see Appendix A). Studies of the local baryonic TFR have shown that galaxies having $V_{\rm flat} \leq 100$ km s^{-1} systematically fall below the TFR defined by more massive galaxies (e.g., McGaugh 2005). However, once the gas fraction is accounted for, all galaxies follow the same *baryonic* TFR. Interpreted that way, our results suggest an evolution of this threshold toward higher masses (velocities) at higher redshifts, of at least $V_{\rm flat} \sim 300$ km s^{-1} at $z \sim 0.6$. This supports the idea that the baryonic TFR would be much more "fundamental" that the stellar-mass TFR (McGaugh 2005).

6. Conclusion

We have studied the evolution of the K-band TFR, using a representative sample of 65 emission line, intermediate-mass galaxies at $z \sim 0.6$, unaffected by field-to-field variations within Poisson statistics, and observed using 3D spectroscopy. We have presented and tested a new method allowing us to safely recover $V_{\rm flat}$ of distant galaxies. We have also investigated possible sources of systematic effects, which can be particularly important when studying the evolution of the TFR. We have paid particular attention to the analysis of both the local and distant samples in as similar as possible ways. We draw the following conclusions:

1. The larger dispersion of the distant TFR is caused by galaxies with anomalous kinematics, ranging from perturbed rotators to very dynamically-disturbed galaxies. We find a positive and strong correlation between the complexity of the kinematics and the scatter contributed to the TF. Once restricted to relaxed rotating disks, the scatter of the TFR

appears to not have evolved, which might suggest no evolution in slope.

2. We detect for the first time a significant evolution of the K-band TFR zero point, which we attribute to an average brightening of $z \sim 0.6$ galaxies by 0.66 ± 0.14 mag. We attribute this evolution to the fact that selected distant galaxies are either starbursts or LIRGs. The distant emission-line rotating disks represent roughly one fourth to one fifth of present-day spiral progenitors, and one half of the whole population of $z \sim 0.6$ intermediate-mass rotating disks (see Paper II). Therefore, a significant part of spiral progenitors are doubling their stellar masses during the last ~6 Gyr, in good agreement with former studies on the evolution of the mass-metallicity relation (Liang et al. 2006), which would suggest no evolution of the baryonic TFR with redshift.
3. Current studies of the evolution of the TFR, even using spatially-resolved kinematics, are limited by important systematic uncertainties, which can be attributed to the limited spatial resolution of the kinematics, and to the derivation of the stellar-mass. These systematic uncertainties represent 20% of the evolution in zero point of the K-band TFR.

Further progress in the study of the evolution of the TFR will benefit from a forthcoming larger sample of RDs. This will allow us to reduce the random uncertainties, allow the slope to vary during the fit, and start studying TF residuals. Although we have limited the local sample to galaxies having a well-defined rotation curve, a decisive answer about the evolution of the TFR will require both local and distant representative samples processed in the same way, from the observational strategy (3D spectroscopy) to the data analysis itself, as we have done in this paper. A similar analysis of a representative local sample observed *using 3D spectroscopy* is required to confirm the above results. This point will be addressed in a future study, using the local kinematic GHASP survey, whose analysis is currently ongoing (Epinat et al. 2008). Finally, an important limitation remains linked to systematic uncertainties, which are mostly due to a lack of spatial resolution. The only way to overcome this limitation will be to develop a new generation of optical integral-field spectrographs with higher spatial-resolution, i.e., assisted by adaptive optics. In this respect, the future extremely large telescopes will allow us to make a decisive leap forward in our understanding of the TFR (Puech et al. 2008).

Acknowledgements. We thank all the GIRAFFE team at the Observatories of Paris and Geneva, and ESO for this unique instrument.

Appendix A: The evolution of the stellar-mass TFR

A.1. The local stellar-mass TFR

Stellar masses $M_{\rm stellar}$ were estimated from $M_{\rm stellar}/L_K$ ratios using the method of Bell et al. (2003). We used a solar luminosity in the $K_{\rm s}$-band of 3.28 (Vega) and assumed a "diet" Salpeter IMF (Bell et al. 2003). This method takes advantage of the tight correlation found between rest-frame optical colors and $M_{\rm stellar}/L_K$ ratios, assuming a universal IMF. These correlations are found to be relatively insensitive to the details of galaxy SFH, dust content, and metallicity (Bell & de Jong 2001; Bell et al. 2003), which implies that they are invaluable for deriving stellar mass without being too sensitive to the details of the stellar population synthesis models. We note that following this method, $M_{\rm stellar}/L_K$ ratios are corrected for the amount of light due to red-giant stars using $g - r$ colors.

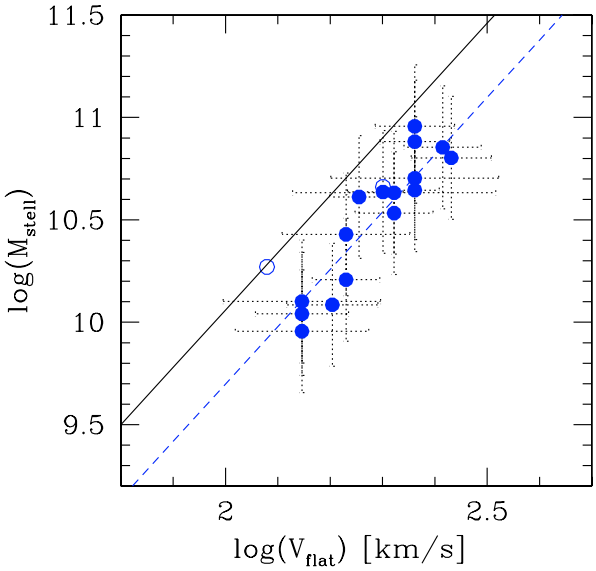

Fig. A.1. Evolution of the stellar-mass TFR in the RD subsample (the two RD+ galaxies are represented with open blue dots). The black line is the local smTFR, while the blue dash-line represents a linear fit to the $z \sim 0.6$ smTFR.

Table A.1. Fits to the local and distant smTFRs, using $\log(M_{\rm stellar}/M_\odot) = a + b \times \log(V_{\rm flat})$.

K-band TFR	Slope a	Zero point b	Comments
Local relation	2.8 ± 0.23	4.46 ± 0.53	SDSS subsample
Distant RDs	2.8	4.10 ± 0.16	Using local slope
Distant RDs	3.28 ± 1.10	3.01 ± 2.47	Slope free
Distant RD/RD+	2.8	4.13 ± 0.15	Using local slope
Distant RD/RD+	2.61 ± 1.33	4.56 ± 3.03	Slope free

According to Bell et al. (2003), using this method, the total random uncertainty on $\log(M_{\rm stellar}/M_\odot)$ at $z \sim 0$ should be lower than 0.1 dex, and the systematic uncertainties due to galaxy ages, dust, or bursts of star-formation can reach 0.1 dex. Finally, the influence of TP-AGB stars in the derivation of stellar masses could result in an overestimation of the stellar mass by ~0.14 dex (Maraston et al. 2006; Pozzetti et al. 2007) in a systematic way.

Using this method, we converted the local K-band TFR in the subsample of the SDSS (see Sect. 2.2) into stellar masses and found:

$$\log(M_{\rm stellar}/M_\odot) = 4.46 \pm 0.53 + (2.8 \pm 0.23) \times \log(V_{\rm flat}), \quad \text{(A.1)}$$

with $\sigma_{\rm res} = 0.15$ dex.

A.2. The distant stellar-mass TFR

To estimate stellar masses in the distant sample (see Table 1), we used the same method as in the local sample, i.e., the K-band luminosity and $B - V$ rest-frame colors. One important issue is whether or not the same correlations between color and $M_{\rm stellar}/L_K$ ratios found at $z = 0$ by Bell et al. (2003) can be directly applied at higher redshift. Borch et al. (2006) showed that this appears possible at least up to $z \sim 0.6$ (see their Fig. 4), with an associated random uncertainty of ~0.3 dex, and an average systematic uncertainty of up to −0.2 dex (i.e., towards an overestimation of the stellar-mass at high z).

We show the derived distant smTFR in Fig. A.1. The smTFR shows the same trend with the kinematic classification as the K-band TFR. Restricting ourselves to RDs, and holding the

Table A.2. Identified systematic uncertainties that could impact the shift of zero point between the local and the distant smTFRs. Systematic uncertainties on $V_{\rm flat}$ have been converted into $M_{\rm stellar}$ using Eq. (A.1). Negative values tend to reduce the shift of zero point, while positive values have the opposite trend.

Description	Bias on $M_{\rm stellar}$ (dex)	Comments
Photometry	∼0	Comparison EIS vs. ACS in the CDFS
M/L_K Evolution with z	+0.1	Following Sect. A.3
IMF Evolution with z	+0.05	Following van Dokkum (2007)
Velocity correction	±0.06	See Sect. 4.2.3
Total	–0.06/+0.21	

slope constant, the distant and local relations have similar dispersions ($\sigma_{\rm res} = 0.12$ dex). If we allow the slope to vary during the fit, we find a residual dispersion of 0.12 dex, suggesting again that assuming no evolution in slope is acceptable. Maintaining the slope at its local value, the distant smTFR zero point is found to be $4.10 \pm 0.16({\rm random})^{+0}_{-0.2}$ (systematic, see above), i.e., 0.36 dex smaller than the local zero point (see Table A.1). A Welcher's t-test gives a probability $\ll 1\%$ that the two relations have the same zero point.

A.3. Stellar-mass systematic uncertainties

The most important systematic uncertainty is that associated with the mass-to-light ratios $[M/L]$ predicted by stellar population synthesis [SPS] models. Absolute values of M/L depend mostly on the SPS model and IMF used, and more particularly on the prescriptions for the TP-AGB stellar-evolution phase (Maraston 2005; Maraston et al. 2006). Pozzetti et al. (2007) compared M/L predictions between Bruzual & Charlot (2003) and Maraston (2005) SPS models and found a systematic difference of −0.14 dex due to different prescriptions for TP-AGB stars. However, they found that this systematic is constant with redshift, at least up to $z \sim 1.2$. In other words, at a given IMF, relative predictions between two different redshifts of SPS models are much more robust in terms of M/L predictions.

We therefore focus in Fig. A.2 on the evolution of $\log(M_{\rm stellar}/L_K)$ between $z \sim 0.6$ and $z = 0$: we show the histograms of $\log(M_{\rm stellar}/L_K)$ derived using the Bell et al. (2003) method, both in the distant and local samples. Both histograms were centered using the median $\log(M_{\rm stellar}/L_K)$ of the local sample: we find that $\log(M_{\rm stellar}/L_K)$ evolves from $z \sim 0.6$ to $z = 0$ by ∼0.06 dex. In this figure, we show other determinations of the evolution of $\log(M_{\rm stellar}/L_K)$ from the literature. Drory et al. (2004), using Maraston (1998) SPS models, found an evolution of 0.13 dex in galaxies with stellar masses between $4 \times 10^{10}\ M_\odot$ and $10^{11}\ M_\odot$, i.e., in a range of stellar-mass similar to GIRAFFE galaxies. This is similar to the 0.15 dex evolution found by Arnouts et al. (2007) in a flux-limited sample over the same redshift range, using Bruzual & Charlot (2003) SPS models. Furthermore, Arnouts et al. (2007) find an evolution of 0.16 dex once restricted to a sample of blue star-forming galaxies. Because such blue galaxies and emission-line galaxies probably belong to the same populations (Hammer et al. 1997), we conclude that we might be underestimating the evolution of $\log(M_{\rm stellar}/L_K)$ by up to ∼0.16–0.06 = 0.1 dex in a systematic way.

What is the origin of this systematic effect? As $\log(M_{\rm stellar}/L_K)$ depends mostly on color and not on mass, Bell et al. (2003) used SPS models to predict their "average" correlations given a reasonable range of SPS parameters (e.g., metallicity, star formation histories). However, Bell et al. (2003) did not explicitly fit the age but assumed instead a reference age of 12 Gyr at $z = 0$. This introduces a systematic difference with other results where age is fitted explicitly. For instance, Drory et al. (2004) find an average age of 8.1 Gyr at $z = 0$. If one compares the median $\log(M_{\rm stellar}/L_K)$ found in the local SDSS sample used in this study, with the average value found by Drory et al. (2004) in a similar mass range, one finds a difference of −0.08 dex (which accounts for the different IMF used). Similarly, we find a difference of −0.16 dex between the median $\log(M_{\rm stellar}/L_K)$ found in the GIRAFFE sample, and the average value found by Drory et al. (2004) at $z = 0.6$. These values are consistent with the systematic error bars quoted above. They suggest that we underestimate the evolution of $\log(M_{\rm stellar}/L_K)$ between $z = 0$ and $z \sim 0.6$ by −0.08 dex, which is consistent with Fig. A.2.

In summary, these comparisons show that we are probably underestimating the evolution of $\log(M_{\rm stellar}/L_K)$ between $z = 0$ and $z \sim 0.6$ by −0.08 dex, and maybe up to −0.1 dex due to the use of the simplified prescriptions for M/L of Bell et al. (2003). This directly translates into a systematic effect of the evolution of smTFR zero point by up to +0.1 dex.

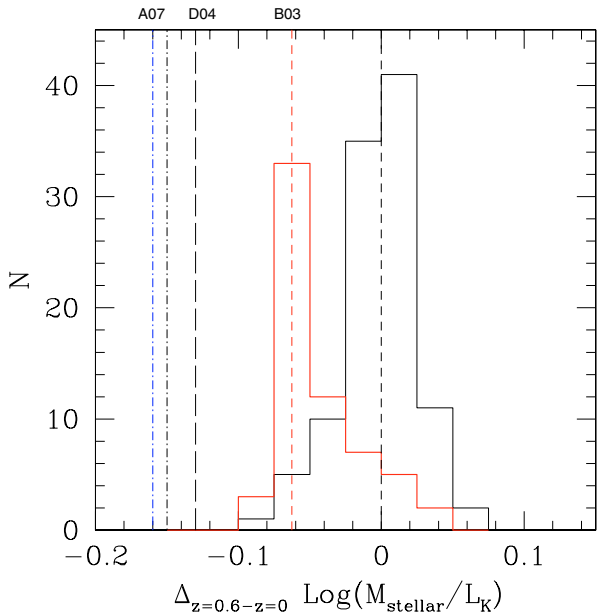

Fig. A.2. Histograms of $\log(M_{\rm stellar}/L_K)$ found in the local and distant samples of galaxies using the method of Bell et al. (2003). Both histograms have been re-centered using the median found in the local samples, which allows us to directly infer the evolution of $\log(M_{\rm stellar}/L_K)$ between $z \sim 0.6$ and $z = 0$, i.e., ∼0.625 dex. Also shown, the evolution of $\log(M_{\rm stellar}/L_K)$ found by Drory et al. (2004) in a sample of intermediate-mass galaxies (black long-dashed line), and Arnouts et al. (2007) in blue star-forming galaxies (blue mixed-line) or independently of the color (black mixed-line).

A.4. Total systematic uncertainty

We summarize all possible sources of systematic uncertainty identified so far in Table A.2. We expressed all in terms of their influence on the shift in the zero point between the distant and the local smTFRs. Taking into account all these uncertainties, we find a shift in the smTFR zero point of $0.36^{0.21}_{-0.06}$ dex between $z \sim 0.6$ and $z = 0$. Systematic uncertainties represent up to ~60% (in dex) of the evolution detected in zero point, i.e., much larger than systematic uncertainties affecting the evolution of the K-band TFR zero point. The derivation of stellar mass is highly model-dependent, which implies a large additional uncertainty. However, we note that these effects tend to overestimate the stellar mass at high redshift, i.e., to minimize the evolution of the smTFR. Using $\log(M_{\rm stellar}/L_K) = \log(M_{\rm stellar}) - \log(L_K)$, one finds that $\log(M_{\rm stellar}/L_K)$ evolves by ~0.1 dex (=0.36−0.66/2.5) between $z \sim 0.6$ and $z = 0$ in the subsample of RDs. Therefore, the evolution in the zero point of the smTFR is quite robust, in the sense that we might have minimized the evolution of $M_{\rm stellar}/L_K$ through the choice of method used to derive the stellar mass (see Sect. A.3).

References

Amram, P., Adami, C., Balkowski, C., et al. 2002, Ap&SS, 281, 393
Arnouts, S., Vandame, B., Benoist, C., et al. 2001, A&A, 379, 740
Arnouts, S., Walcher, C. J., Le Fèvre, O., et al. 2007, A&A, submitted [arXiv:astro-ph/0705.2438]
Atkinson, N., Conselice, C. J., & Fox, N. 2007, MNRAS, submitted [arXiv:astro-ph/0712.1316]
Bamford, S. P., Aragon-Salamanca, A., & Milvang-Jensen, B. 2006, MNRAS, 366, 308
Bell, E. F., & de Jong, R. S. 2001, ApJ, 550, 212
Barnes, J. E. 2002, MNRAS, 333, 481
Bell, E. F., McIntosh, D. H., Katz, N., & Weinberg, M. D. 2003, ApJS, 149, 289
Bell, E. F., Papovich, C., Wolf, C., et al. 2005, ApJ, 625, 23
Bell, E. F., Zheng, X. Z., Papovich, C., et al. 2007, ApJ, 663, 834
Birnboim, Y., Dekel, A., & Neisten, E. 2007, MNRAS, submitted [arXiv:astro-ph/0703435]
Blanton, M. R., Schlegel, D. J., Strauss, M. A., et al. 2005, AJ, 129, 2562
Böhm, A., & Ziegler, B. L. 2007, ApJ, 668, 846
Böhm, A., Ziegler, B. L., Saglia, R. P., et al. 2004, A&A, 420, 97
Borch, A., Meisenheimer, K., Bell, E. F., et al. 2006, A&A, 453, 869
Bruzual, G., & Charlot, S. 2003, MNRAS, 244, 1000
Carignan, C., Chemin, L., Huchtmeier, W. K., & Lockman, F. J. 2006, ApJ, 641, 109
Carpenter, J. M. 2001, AJ, 121, 2851
Chemin, L., Balkowski, C., Cayatte, V., et al. 2006, MNRAS, 366, 812
Chiu, K., Bamford, S. P., & Bunker, A. 2007, MNRAS, 377, 806
Conselice, C. J., Bundy, K., Ellis, R. S., et al. 2005, ApJ, 628, 160
Conroy, C., Prada, F., Newman, J. A., et al. 2007, ApJ, 654, 153
Courteau, S. 1997, AJ, 114, 2402
Davé, R. 2007, MNRAS, submitted [arXiv:astro-ph/0710.0381]
De Rijcke, S., Zeilinger, W. W., Hau, G. K. T., et al. 2007, ApJ, 659, 1172
Dekel, A., & Birnboim, Y. 2006, MNRAS, 368, 2
Dickinson, M., Papovich, C., Ferguson, H. C., et al. 2003, ApJ, 587, 25
Drory, N., Bender, R., Feulner, G., et al. 2003, ApJ, 595, 698
Drory, N., Bender, R., Feulner, G., et al. 2004, ApJ, 608, 742
Dutton, A. A., van den Bosch, F. C., Dekel, A., et al. 2007, ApJ, 654, 27
Ellis, R. 1997, ARA&A, 25, 389
Epinat, B., Amram, P., Marcelin, M., et al. 2008, MNRAS, submitted
Flores, H., Hammer, F., Puech, M., Amram, P., & Balkowski, C. 2006, A&A, 455, 107
Franceschini, A., Rodighiero, G., Cassata, P., et al. 2006, A&A, 453, 397
Governato, F., Willman, B., Mayer, L., et al. 2007, MNRAS, 374, 1479
Hammer, F., Flores, H., Lilly, S. J., et al. 1997, ApJ, 481, 49
Hammer, F., Gruel, N., Thuan, T. X., et al. 2001, ApJ, 550, 570
Hammer, F., Flores, H., Elbaz, D., et al. 2005, A&A, 430, 115
Hammer, F., Puech, M., Chemin, L., Flores, H., & Lehnert, M. 2007, ApJ, 662, 322
Hogg, D. W. 1999 [arXiv:astro-ph/9905116]
Kannappan, S. J., & Barton, E. J. 2004, AJ, 127, 2694
Kassin, S. A., Weiner, B. J., Faber, S. M., et al. 2007, ApJ, 660, 35
Keres, D., Katz, N., Weinberg, D. H., & Davé, R. 2005, MNRAS, 363, 2
Kroupa, P. 2001, MNRAS, 322, 231
Liang, Y. C., Hammer, F., & Flores, H. 2006, A&A, 447, 113
Maraston, C. 1998, MNRAS, 300, 872
Maraston, C. 2005, MNRAS, 362, 799
Maraston, C., Daddi, E., Renzini, A., et al. 2006, ApJ, 652, 85
Mason, E., Kaufer, A., & Hainaut, O. 2007, ISAAC Instrument data reduction cookbook
McGaugh, S. S. 2005, ApJ, 632, 859
Mo, H. J., Mao, S., & White, D. M. 1998, MNRAS, 295, 319
Neichel, B., et al. 2008, A&A, submitted
Noordermeer, E., & Verheijen, M. A. W 2007, MNRAS, accepted [arXiv:0708.2822]
Okamoto, T., Eke, V. R., Frenk, C. S., & Jenkins, A. 2005, MNRAS, 363, 1299
Persic, M., & Salucci, P. 1991, ApJ, 368, 60
Persson, S. E., Murphy, D. C., Krzeminski, W., et al. 1998, AJ, 116, 2475
Pizagno, J., Prada, F., Weinberg, D. H., et al. 2007, AJ, 134, 945
Portinari, L., & Sommer-Larsen, J. 2007, MNRAS, 375, 913
Press, W. H. 2002, Numerical recipes in C++: the art of scientific computing (Cambridge University Press)
Puech, M., Flores, H., Hammer, F., & Lehnert, M. D. 2006a, A&A, 455, 131
Puech, M., Hammer, F., Flores, H., Östlin, G., & Marquart, T. 2006b, A&A, 455, 119
Puech, M., Hammer, F., Lehnert, M. D., & Flores, H. 2007a, A&A, 466, 83
Puech, M., Hammer, F., Flores, H., et al. 2007b, A&A, accepted [arXiv:0711.0611]
Puech, M., Flores, H., Lehnert, M. D., et al. 2008, MNRAS, submitted
Pozzetti, L., Bolzonella, M., Lamareille, F., et al. 2007, A&A, 474, 443
Ravikumar, C. D., Puech, M., Flores, H., et al. 2007, A&A, 465, 1099
Robertson, B., Bullock, J. S., Cox, T. J., et al. 2006, ApJ, 645, 986
Russell, D. G. 2004, ApJ, 607, 241
Saintonge, A., Masters, K. L., Marinoni, C., et al. 2007, A&A, submitted [arXiv:0710.0760]
Salpeter, E. E. 1955, ApJ, 121, 161
Simard, L., & Pritchet, C. J. 1998, ApJ, 505, 96
Tully, R., & Fisher, J. 1977, A&A, 54, 661
Tully, R., & Fouqué, P. 1985, ApJS, 58, 67
Tully, R., Pierce, M. J., Huang, J., et al. 1998, AJ, 115, 2264
van der Wel, A., Holden, B. P., Franx, M., et al. 2007, submitted [arXiv:0707.2787]
van Dokkum, P. G. 2007, ApJ, submitted [arXiv:astro-ph/0710.0875]
Verheijen, M. A. W. 2001, ApJ, 563, 694
Vogt, N., Herter, T., Haynes, M. P., et al. 1993, ApJ, 415, 95
Vogt, N., Forbes, D. A., Philips, A. C., et al. 1996, ApJ, 465, 15
Vogt, N., Philips, A. C., Faber, S. M., et al. 1997, ApJ, 479, 121
Weiner, B. J., Willmer, C. N. A., Faber, S. M., et al. 2006, ApJ, 653, 1027
Yang, Y., Flores, H., Hammer, F., et al. 2007, A&A, accepted [arXiv:0711.2305]